Indian Institute of Science Education and Research Bhopal

SUMMER INTERNSHIP PROGRAM 2025

Exploring Magnetic Dynamics: Experimental FMR and the Theory of ST-FMR

PROJECT REPORT

Report By:

Abhay Saxena
Email: saxenabhay@outlook.com
Fourth Year BS-MS,
Department of Physical Sciences,
IISER Kolkata

Mentor:

Dr. Kuntal Roy
Email: kuntal@iiserb.ac.in
Assistant Professor,
Electrical Engineering and Computer Science Department,
IISER Bhopal

Submitted: Sunday 7th September, 2025

Acknowledgements

Thanks to my parents for their unconditional love and belief in me.

My deepest gratitude goes to Professor Kuntal Roy, my mentor and guide, for his unwavering support and tireless dedication. This project, the establishment of the Ferromagnetic Resonance (FMR) setup from its foundation, could come to fruition only because of him. Professor Roy was a true hands-on mentor, working alongside me day and night and patiently guiding me through every step. From the fundamentals of LabVIEW, joining BNC circuits and soldering to nuanced equipment safety protocols, he instilled in me the core principles of experimental science. He generously shared a wealth of resources, and taught me the critical mindset of experimental thinking and the importance of maintaining lab manuals and keeping a track of the progress.

Thanks to Siva and Sarthak for helping integrate Lock-in, Nanovoltmeter, picoammeter and gauss probe into labview. Very grateful to Mithesh Nanda for helping me setup the experiment and taking up the work ahead. Labmates at Spintronics lab with their camaraderie and insights were a constant source of support, making the lab a collaborative and encouraging environment.

I would also like to thank all my friends at the institute of IISER Bhopal for making it a memorable stay for me.

Abstract

This work serves as both a practical guide to basic Ferromagnetic Resonance (FMR) setup and a theoretical primer for Spin-Torque Ferromagnetic Resonance (ST-FMR). It begins with an exploration of various FMR experimental techniques, including setups based on spectrum analyzers, nanovoltmeters and most importantly, is focused on lock-in amplifiers. The report then transitions to a theoretical study of spintronics, detailing the fundamental concepts necessary to understand the principles behind ST-FMR and establishing an experimental setup for same.

Contents

Chapter 1

Fundamentals of FMR

Most of the theory is based on the book by C.Kittel [6] and lecture notes, by Dr. Kuntal Roy, for Spintronics Course at IISER Bhopal.

1.1 Magnetic Domains

To describe fermions (like electrons), we need antisymmetric wavefunction ($\Psi(1,2) = -\Psi(2,1)$).

$$\chi_s = \frac{1}{\sqrt{2}} \left(|\uparrow_1\downarrow_2\rangle - |\downarrow_1\uparrow_2\rangle \right).$$

Hence,
Singlet spin state (antisymmetric, total spin $S = 0$):

$$\chi_s = \frac{1}{\sqrt{2}} \left(|\uparrow_1\downarrow_2\rangle - |\downarrow_1\uparrow_2\rangle \right).$$

i.e. Symmetric spatial wavefunction paired with an antisymmetric spin wavefunction.
Triplet spin states (symmetric, total spin $S = 1$):

$$\chi_t = \begin{cases} |\uparrow_1\uparrow_2\rangle, \\ \frac{1}{\sqrt{2}} \left(|\uparrow_1\downarrow_2\rangle + |\downarrow_1\uparrow_2\rangle \right), \\ |\downarrow_1\downarrow_2\rangle. \end{cases}$$

i.e. Antisymmetric spatial wavefunction paired with a symmetric spin wavefunction (triplet state).

Example of Helium for Heisenberg Exchange Hamiltonian

Consider two electrons in a system (e.g., in a molecule like H_2 or a solid). The non-relativistic Hamiltonian is:

$$\hat{H} = -\frac{\hbar^2}{2m}(\nabla_1^2 + \nabla_2^2) + V(\vec{r}_1) + V(\vec{r}_2) + \frac{e^2}{4\pi\epsilon_0|\vec{r}_1 - \vec{r}_2|}$$

where $V(\vec{r}_i)$ is the external potential (from nuclei here), and the last term is the Coulomb repulsion between electrons. If we compute the expectation value of the Hamiltonian $\langle\Psi|\hat{H}|\Psi\rangle$ for the singlet and triplet states, we notice, only the last coulumbic interaction term is different for singlet and triplet case.

$$\langle\phi_s|\frac{e^2}{4\pi\epsilon_0|\vec{r}_1 - \vec{r}_2|}|\phi_s\rangle \quad \text{vs.} \quad \langle\phi_t|\frac{e^2}{4\pi\epsilon_0|\vec{r}_1 - \vec{r}_2|}|\phi_t\rangle$$

We call this as the **exchange term**. This braket (integral) for both cases can be given as:

$$K = \int d^3r_1 d^3r_2 \, \phi_1^*(\vec{r}_1)\phi_2^*(\vec{r}_2)\frac{e^2}{4\pi\epsilon_0|\vec{r}_1 - \vec{r}_2|}\phi_2(\vec{r}_1)\phi_1(\vec{r}_2)$$

The energy difference between singlet and triplet states is:

$$E_s - E_t = 2K$$

where E_s is the singlet energy and E_t is the triplet energy. The triplet state is lower in energy by $2K$.

Hence, For a system of two electrons with spins $\vec{S}_1$, effective spin Hamiltonian that reproduces this energy difference is:

$$\hat{H}_{ex} = -2J\vec{S}_1 \cdot \vec{S}_2$$

A generalization of the same for many-electron system is called **Heisenberg Exchange Hamiltonian** (approximation):

$$\boxed{\hat{\mathbb{H}}_{ex} = -2 \sum_{i<j(i\neq j)} \vec{J}_{ij}\vec{S}_i \cdot \vec{S}_j} \tag{1.1}$$

Here $\vec{J}_{ij}$ is the *exchange constant* for the pair of electrons i and j and $\vec{S}$ being the spin operators (S = 1/2 for electron).[6] for a 3d lattice case, these spin operators obey the angular momentum commutation relation:

$$[S_j^x, S_j^y] = i\sum_z \varepsilon_{xyz} S$$

and different sites spins, commuting.The magnetization of a ferromagnet comes from the quantum mechanical alignment of electron spins in its atoms, not from free electrons. This exchange interaction forces the magnetic moments of neighboring electrons to align in a parallel fashion below Curie point. If $\vec{J}_{ij}$ ***is negative*** $\rightarrow$ ***Ferromagnetic.*** since interaction energy of two spins favors them to be parallel in this case, it creates macroscopic magnetization vectors called **magnetic domains**, whose moment is represented by $\vec{M}$. All the dynamics described ahead would be considering these magnetic domains, and not exactly spins, whose moment can be given by $\vec{\mu}$.

$$\vec{M} = \frac{1}{V}\sum_i \vec{\mu_i} \tag{1.2}$$

with V being volume of the whole material and $\sum_i \vec{\mu_i}$ being vector sum of individual magnetic moments of spins.

1.2 Landau-Lifshitz-Gilbert (LLG) Equation

we can then assume when an electron is placed in an applied magnetic field $\vec{H}$, the magnetic field will produce a torque (τ) on the magnetic moment $\vec{\mu}$:

$$\vec{\mu} \times \vec{H} = \tau = \frac{d\vec{L}}{dt} \tag{1.3}$$

where $\vec{L}$ is the angular momentum of the electrom. Also,

$$\vec{\mu} = I \cdot \vec{A}.$$

Since, for one time period T, $I = -e/t$ and $A = \pi r^2$, we see,

$$\vec{\mu} = -\frac{e}{T} \cdot \pi r^2 \cdot \hat{A} \tag{1.4}$$

Also,

$$\vec{L} = m \cdot \omega r^2 = m_e \cdot 2\pi f r^2 = \frac{m_e \cdot 2\pi \cdot r^2}{T}\hat{L}$$

Replacing which in (1.4), gives us,

$$\vec{\mu} = -\frac{e}{2m_e}\vec{L}$$

because, $\hat{A} = \hat{L}$. lets call for ease,

$$\gamma = \frac{e}{2m_e},$$

However, we are imagining the electron to be a rigid body rotation around an axis, which is not really the case, since the mass in not distributed identically to charge in such a model. Infact it is close to twice what is predicted by this *classical model*. Hence we introduce a correction factor called as **Landé g-factor** defined to be the ratio of magnetic moment of a particle to its total angular momentum, which is close to 2 for electron. Hence we redefine:

$$\boxed{\gamma = \frac{g_e e}{2m_e} = \frac{g_e \cdot \mu_b}{\hbar},} \tag{1.5}$$

also known as the ***gyromagnetic ratio*** so, we may define it is:

$$\gamma = \frac{\vec{M}}{\vec{S}} = \frac{\text{magnetic moment}}{\text{angular momentum}}$$

Hence, we say:

$$\vec{\mu} = -\gamma\vec{L} \tag{1.6}$$

replacing the same, in (1.3), we get [22]:

$$\vec{\mu} \times \vec{H}_{eff} = \tau = -\frac{1}{\gamma}\frac{d\vec{\mu}}{dt} \tag{1.7}$$

or, for all the magnetic moments combined with $\vec{M} = N\vec{\mu}$, as:

$$\frac{d\vec{M}}{dt} = -\gamma\vec{M} \times \vec{H}_{eff} \tag{1.8}$$

Being the **equation describing the precession**. Also, we can further say, it is valid for unit vector $\hat{M}$, hence describing the angular velocity as:

$$\omega = \gamma B$$

or simply,

$$f = \frac{\gamma}{2\pi}B \tag{1.9}$$

Describing **natural frequency of rotation**. However, this is ideal case scenario where spins precess forever. We hence need to introduce damping term to account for dissipation of energy from the precessing magnetization to its surroundings.

Origin of Damping and Incorporation Through LLG

Most fundamental origin of this damping is:

- **Spin-orbit coupling**: We can derive SOC directly from non-relativistic limit of Dirac equation to see the classical picture, revealing Zeeman interaction and SOC. Precession generates a time varying spin orientation of electrons, which is coupled to the electrons orbital motion due to the relativistic effects of SOC. This orbal momentum is then lost to *heat* directly (collisions).

- **Spin lattice relaxation**: Since spins are magnetic and phonons electric, hence, spin-phonon coupling is pretty weak and is mostly mediated by SOC only. Due to interaction of these excited electrons with **phonons**, energy is transfered to lattice, which inturn is dissipated as *heat*.

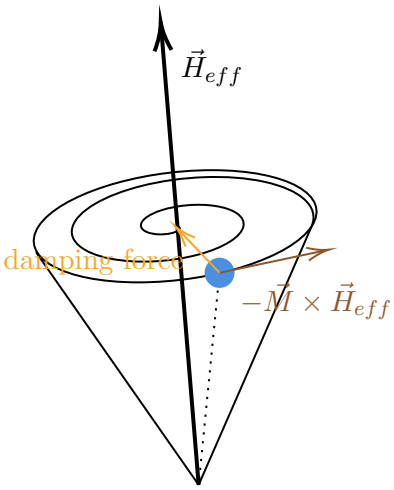

Figure 1.1: Spin precession and damping force direction.

There are various ways to incorporate this extra damping term to (1.8). Originally, the **Landau-Lifshitz form** can be described as:

$$-\lambda \vec{M} \times \vec{M} \times \vec{H}_{eff} \tag{1.10}$$

with M_s being the **Saturation Magnetization** of the sample and α being the dimensionless constant called as **damping factor** as we will notice in LLG. This gives the final **Landau-Lifshitz equation** as:

$$\boxed{\frac{dM}{dt} = -\gamma_0 \vec{M} \times \vec{H}_{eff} - \lambda \vec{M} \times \vec{M} \times \vec{H}_{eff}} \tag{1.11}$$

Which is not hard to imagine as being the force always perpendicular to the precessing direction. However, we can actually look at it more intuitively by assuming it directly as the damping term to be rate of change of $\vec{M}$ cross product with $\vec{M}$ as can be given by **Gilbert form** of damping:

$$\frac{\alpha}{M_s} \vec{M} \times \frac{d\vec{M}}{dt} \tag{1.12}$$

giving the final **Landau-Lifshitz-Gilbert equation** as:

$$\boxed{\frac{dM}{dt} = -\gamma \vec{M} \times \vec{H}_{eff} + \frac{\alpha}{M_s} \vec{M} \times \frac{d\vec{M}}{dt}} \tag{1.13}$$

being relatively more intuitive as it is cross product of rate of retardation with M, always pointing perpendicular to $\hat{B}$. Both the formulae account for same equation with different constants.

LLG to LL equation conversion

Start from the Gilbert form

$$d\vec{M}/dt = -\gamma\, \vec{M} \times \vec{H}_{\text{eff}} + \frac{\alpha}{M_s}\, \vec{M} \times (d\vec{M}/dt).$$

Bring the damping term to the left:

$$\big(I - \tfrac{\alpha}{M_s}\,\vec{M}\times\big)d\vec{M}/dt = -\gamma\,\vec{M}\times\vec{H}_{\text{eff}}. \tag{1.14}$$

Apply $\vec{M}\times$ to the above equation. Using the triple-product identity $\vec{M}\times(\vec{M}\times X) = \vec{M}(\vec{M}\cdot X) - \vec{M}^2 X$ and $\vec{M}\cdot(d\vec{M}/dt) = \frac{1}{2}d(\vec{M}\cdot\vec{M})/dt = 0$ (since M_s is constant), we get $\vec{M}\times(\vec{M}\times d\vec{M}/dt) = -M_s^2 d\vec{M}/dt$. Therefore

$$\big(\vec{M}\times + \alpha M_s I\big)d\vec{M}/dt = -\gamma\,\vec{M}\times(\vec{M}\times\vec{H}_{\text{eff}}). \tag{2}$$

Now combine (1.14) with $\frac{\alpha}{M_s}\times$(2):

$$\Big(I - \tfrac{\alpha}{M_s}\,M\times\Big)d\vec{M}/dt + \frac{\alpha}{M_s}\Big(\vec{M}\times + \alpha M_s I\Big)d\vec{M}/dt = -\gamma\Big(\vec{M}\times\vec{H}_{\text{eff}} + \frac{\alpha}{M_s}\vec{M}\times(\vec{M}\times\vec{H}_{\text{eff}})\Big).$$

The left-hand side simplifies to $(1+\alpha^2)d\vec{M}/dt$, so

$$(1+\alpha^2)\,d\vec{M}/dt = -\gamma\Big(\vec{M}\times\vec{H}_{\text{eff}} + \frac{\alpha}{M_s}\vec{M}\times(\vec{M}\times\vec{H}_{\text{eff}})\Big).$$

Finally divide by $1+\alpha^2$ to obtain the Landau-Lifshitz form:

$$d\vec{M}/dt = -\frac{\gamma}{1+\alpha^2}\,\vec{M}\times\vec{H}_{\text{eff}} \;-\; \frac{\alpha\gamma}{M_s(1+\alpha^2)}\,\vec{M}\times\big(\vec{M}\times\vec{H}_{\text{eff}}\big).$$

notice that,

$$\boxed{\begin{aligned}\gamma_0 &= \frac{\gamma}{1+\alpha^2}\\ \lambda &= \frac{\alpha\gamma}{M_s(1+\alpha^2)}\end{aligned}} \tag{1.15}$$

Can be used to go from LL to LLG equation.

1.3 Core idea of FMR

Basic idea behind FMR is that we keep increasing the $\vec{H}_{eff}$ by increasing an external $\vec{B}_{ext}$ while throwing an antidamping microwave on sample in perpendicular plain. When the anti-damping has same frequency as the natural frequency (1.9), we see that damping stops, leading to sample using up the microwave and hence absorbing power.This absorbed power should ideally be just at the $\vec{B}_{ext}$ when it is exactly same as thrown microwave, but in truth, we see a Lorentzian power Absorption for B vs Absorption. Reason for the same is discussed in section 1.4. Complete working will be discussed in chapter 3. Ideally the images we see for FMR look like derivative of Lorentzian, explanation of which is in section 1.5. Given in Figure 1.2, we can see that the sample is kept on a Coplanar waveguide (CPW). We basically use it to allow microwave to pass through the sample's surface, resonsible for antidamping. Then the whole CPW is kept between an electromagnet to generate external $\vec{B}$ responsible for the larmor precession.

1.4 Susceptibility Tensor and Lorentzian Absorption

Proof that power absorption is proportional to $\Im(\chi_{xx})$

To explain this absorption shape, we look at Polder Susceptibility [13][6]. In macroscopic electrodynamics, the instantaneous power density transferred from the RF field to the magnetization is

$$p_M(t) = \mu_0\,\vec{H}(t)\cdot\frac{d\vec{M}(t)}{dt}. \tag{1.16}$$

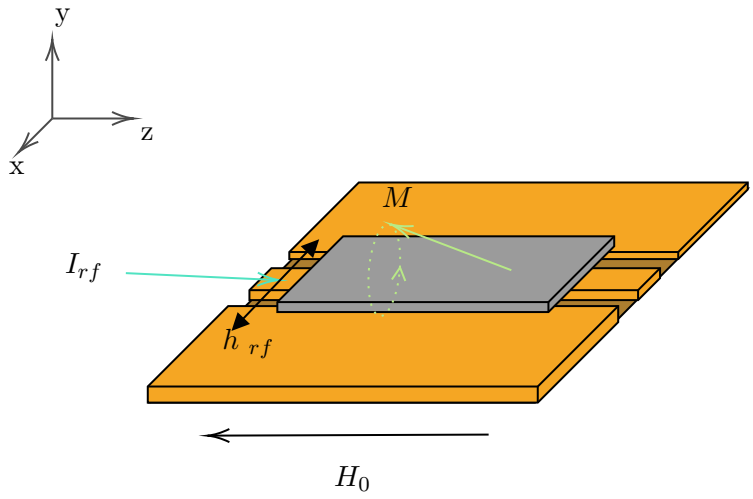

Figure 1.2: Sample on CPW with microwave passing through the surface. Whole thing is kept in External H_0. (inspiration: [4])

Because, the dipole moment's potential is $U = -m \cdot \mathbf{B}$, and $p_M(t) = \frac{dU}{dt} = -\mathbf{m} \cdot \frac{d\mathbf{B}}{dt}$. Replacing $B = \mu_0(H + M)$ isolates the non-returned piece $\mu_0 H \cdot \partial M/\partial t$.

Assume time-harmonic fields with phasors $\vec{h}(t) = \Re\{\vec{h}\, e^{-i\omega t}\}$ and $\vec{m}(t) = \Re\{\vec{m}\, e^{-i\omega t}\}$, related by linear response $\vec{m} = \boldsymbol{\chi}\, \vec{h}$. Averaging over one period,

$$\left\langle \vec{h}(t) \cdot \dot{\vec{m}}(t) \right\rangle = \frac{\omega}{2}\, \Im\big(\vec{h}^* \cdot \vec{m}\big) = \frac{\omega}{2}\, \Im\big(\vec{h}^* \cdot \boldsymbol{\chi}\, \vec{h}\big),$$

which follows by writing

$$\vec{h}(t) = \tfrac{1}{2}(\vec{h} e^{-i\omega t} + \vec{h}^* e^{i\omega t})$$
$$\dot{\vec{m}}(t) = \tfrac{1}{2}(-i\omega\, \vec{m} e^{-i\omega t} + i\omega\, \vec{m}^* e^{i\omega t})$$

and discarding oscillatory terms at $\pm 2\omega$ in the time average. Therefore, the cycle-averaged absorbed power density is

$$P \equiv \langle p_M \rangle = \frac{1}{2}\, \omega\, \mu_0\, \Im\big(\vec{h}^* \cdot \boldsymbol{\chi}\, \vec{h}\big). \tag{1.17}$$

For an in-plane drive $\vec{h} = h_x \hat{\vec{x}}$, this reduces to

$$\boxed{P = \frac{1}{2}\, \omega\, \mu_0\, \Im(\chi_{xx})\, |h_x|^2.} \tag{1.18}$$

so absorption is proportional to the imaginary part $\Im(\chi_{xx})$. Also notice that **generally larger or thicker samples absorb more power** due to increased magnetic volume and eddy-current effects, enhancing FMR signal as we have just proved, for power absorbed per unit volume. However, note that the thickness is limited by microwave skin depth (typically $\sim 1 - 10\mu m$ at GHz frequencies) i.e. microwave travels only at the surface in contact with the CPW[3].

Finding the χ''_{xx}

We start from the Landau–Lifshitz–Gilbert (LLG) equation for magnetization $\vec{M}$ in a ferromagnet with effective field $\vec{H}_{\text{eff}}$. We consider a DC bias $\vec{H}_0 = H_0 \hat{y}$, a small RF field

$$\vec{h}(t) = h_x \hat{x} + h_z \hat{z}$$

with time dependence $e^{i\omega t}$, and write

$$\vec{M} = m_x \hat{x} + M_s \hat{y} + m_z \hat{z}$$

with $m_{x,z} \ll M_s$. Putting in the LLG equation, The effective field includes external, anisotropy, and demagnetizing contributions:

$$\vec{H}_{\text{eff}} = \vec{H}_0 + \vec{h}(t) + \vec{H}_k + \vec{H}_d, \qquad \vec{H}_k = \frac{H_k}{M_s} m_z \hat{z}, \quad \vec{H}_d = -m_z \hat{z}.$$

Linearizing (neglecting terms like $m_i h_j$ and $m_i m_j$) gives

$$-i\omega \begin{pmatrix} m_x \\ m_z \end{pmatrix} = -\gamma\mu_0 \begin{pmatrix} M_s h_z + (H_k - M_s - H_0)\, m_z \\ -M_s h_x + H_0\, m_x \end{pmatrix} - i\omega \frac{\alpha}{M_s} \begin{pmatrix} M_s m_z \\ -M_s m_x \end{pmatrix}. \tag{1.19}$$

Rearranging to matrix form:

$$\begin{pmatrix} -i\omega & -\gamma\mu_0(H_k - M_s - H_0) - i\omega\alpha \\ \gamma\mu_0 M_s + i\omega\alpha & -i\omega \end{pmatrix} \begin{pmatrix} m_x \\ m_z \end{pmatrix} = -\gamma\mu_0 \begin{pmatrix} M_s h_z \\ -M_s h_x \end{pmatrix}.$$

Equivalently, the component equations are

$$-i\omega m_x = -\gamma\mu_0 \big[M_s h_z + (H_k - M_s - H_0) m_z \big] - i\omega\alpha\, m_z,$$

$$-i\omega m_z = -\gamma\mu_0 \big[-M_s h_x + H_0 m_x \big] + i\omega\alpha\, m_x.$$

In a compact driving form:

$$\begin{pmatrix} i\omega & \gamma\mu_0(H_0 + M_s - H_k) + i\omega\alpha \\ -\gamma\mu_0 H_0 - i\omega\alpha & i\omega \end{pmatrix} \begin{pmatrix} m_x \\ m_z \end{pmatrix} = \gamma\mu_0 M_s \begin{pmatrix} h_z \\ h_x \end{pmatrix}.$$

For in-plane RF drive h_x (set $h_z = 0$), we write $\vec{m} = \boldsymbol{\chi}\, \vec{h}$. One convenient form relates $\vec{h}$ and $\vec{m}$ as

$$\vec{h} = \frac{1}{\gamma\mu_0 M_s} \begin{pmatrix} \gamma\mu_0 H_0 - i\omega\alpha & -i\omega \\ i\omega & \gamma\mu_0(H_0 + M_s - H_k) - i\omega\alpha \end{pmatrix} \vec{m}.$$

Inverting gives the Polder susceptibility. Defining $M_{\text{eff}} = M_s - H_k$ (sign convention varies from the source), a standard explicit form for χ_{xx} is [4].

$$\chi_{xx}(\omega, H_0) = \frac{M_s \big(H_0 + M_{\text{eff}} - i\, \frac{\alpha\omega}{\gamma\mu_0} \big)}{H_0(H_0 + M_{\text{eff}}) - \Big(\frac{\omega}{\gamma\mu_0} \Big)^2 - i\, \frac{\alpha\omega}{\gamma\mu_0}(2H_0 + M_{\text{eff}})}. \tag{1.20}$$

An equivalent parametrization often used in derivations introduces

$$\chi_{xx} = \frac{M_s \big(A + i\, \alpha\, \frac{\omega}{\gamma} \big)}{\big(A + i\, \alpha\, \frac{\omega}{\gamma} \big) \big(B + i\, \alpha\, \frac{\omega}{\gamma} \big) - \Big(\frac{\omega}{\gamma} \Big)^2}, \quad A = H_0 + H_u, \quad B = H_0 + M_{\text{eff}}.$$

and with $\Delta H = 2\, \frac{\alpha\omega}{\gamma\mu_0}$ one can also write the damping term in the denominator as $-\, i\, \frac{\Delta H}{2}\, (2H_0 + M_{\text{eff}})$. Let

$$D \equiv H_0(H_0 + M_{\text{eff}}) - \Big(\frac{\omega}{\gamma\mu_0} \Big)^2 + i\, \frac{\alpha\omega}{\gamma\mu_0}(2H_0 + M_{\text{eff}}), \quad N \equiv M_s \big(H_0 + M_{\text{eff}} + i\, \frac{\alpha\omega}{\gamma\mu_0} \big),$$

so that $\chi_{xx} = N/D$. For small α, $N \approx M_s(H_0 + M_{\text{eff}})$ and

$$\Im(\chi_{xx}) = -\, M_s(H_0 + M_{\text{eff}})\, \frac{\frac{\alpha\omega}{\gamma\mu_0}(2H_0 + M_{\text{eff}})}{\big[H_0(H_0 + M_{\text{eff}}) - \big(\frac{\omega}{\gamma\mu_0} \big)^2 \big]^2 + \Big[\frac{\alpha\omega}{\gamma\mu_0}(2H_0 + M_{\text{eff}}) \Big]^2}. \tag{1.21}$$

Which is nothing but a Lorentzian equation

$$L(x) = \frac{1}{\pi} \cdot \frac{\Gamma/2}{(x - x_0)^2 + (\Gamma/2)^2}$$

So basically we have proved that absorption in FMR when plotting ω vs Absorption is Lorentzian. Also $\omega = \gamma H$, so when plotting magnetic field against absorption, we should again see a Lorentzian.

It is interesting to note that these results are valid even at zero B. This implies that the **FMR output could even be across $B_{ext} = 0$ point!** The peak, however, could not occur at $B_{ext} = 0$. Implying there would be resonance like behaviour in few domains, despite having no magnetic field, and just the anti-damping force.

1.5 Modulation-Induced Derivative

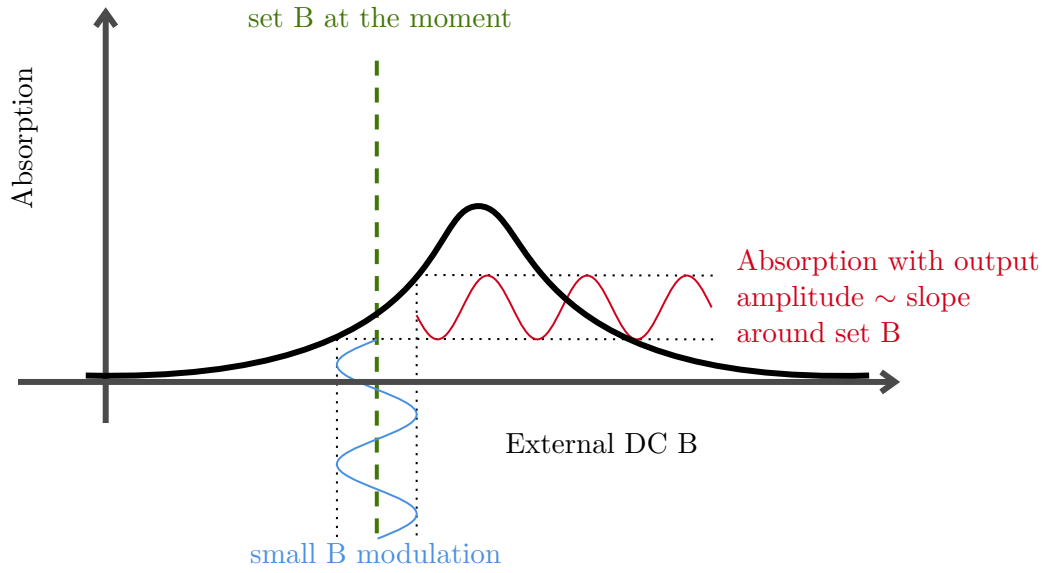

Figure 1.3: Variation of absorption with Modulation in B captured by Lock-in (inspiration: [5])

Generally, we are not able to directly measure the absorption from the sample directly due to a lot of noise, especially $1/f$ noise from the components of the experimental setup. Hence, we instead modulate the H_{DC} with an H_{AC} on top of it, with a frequency is high enough to avoid $1/f$, but not in microwave region. Generally, around 200–100k Hz. This modulation is a small fluctuation in H_{DC} in the same direction. We then capture the amplitude of this oscillation using a lock-in amplifier, discussed in detail in section 2.1. Small B oscillation generates an absorption output which itself oscillates at same frequency as the modulation, with amplitude proportional to the slope around the set H_{DC}. This is explained visually, via Figure 1.3. We then observe an output which rather looks like the derivative of the Lorentzian as described in Figure 1.4.

1.6 Kittel Equation

it is not hard to see from (1.21), by comparing it to the Lorentzian equation, that the center of this Lorentzian, where resonance should be situated is at the peak, around the center x_0, which is at,

$$\omega_{\text{res}} = \gamma\mu_0\sqrt{H_0\big(H_0 + M_{\text{eff}}\big)}. \tag{1.22}$$

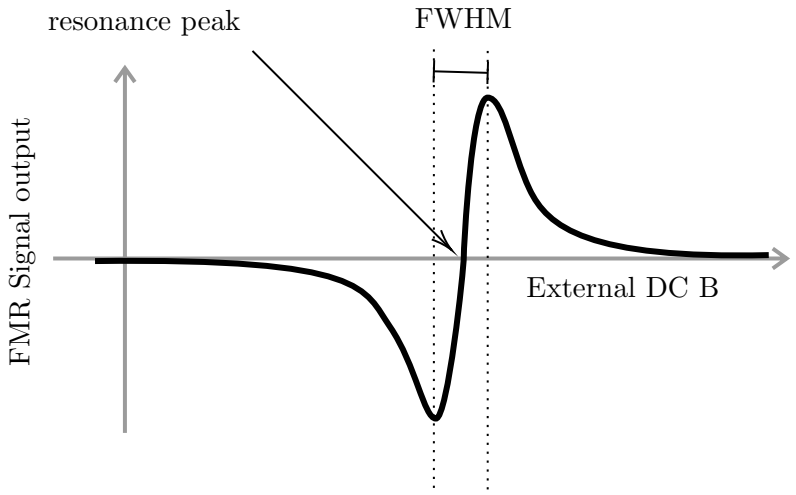

Figure 1.4: Derivative of the Lorentzian, the expected output from a Lock-in Amplifier. Given is the in phase output for direct FMR and out-of-phase output for absorption peak.

$$\chi''_{xx}(\Delta) \approx \frac{\text{const}}{\Delta^2 + \Gamma^2}, \qquad \Gamma \propto \frac{2\alpha\omega}{\gamma\mu_0} = \Delta H. \tag{1.23}$$

We also already know this Γ is nothing but the FWHM of any Lorentzian equation and hence, we can determine both α and ω_{res}, from any FMR measurement. For the case, where modulation is involved, we may simply look at the peaks of the derivative output, distance between which, will give us the FWHM and the peak is, as obvious, at the point, it passes through zero (see: Figure 1.4). Note that these equations let us predict that at higher frequencies, generally the

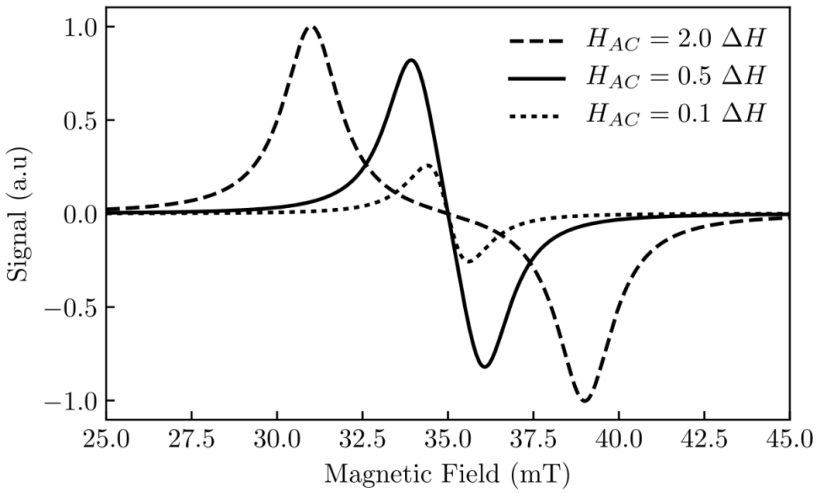

Figure 1.5: Derivative dependence on Modulation size (source: [4]). Notice how signal is ideally supposed to be closer to $0.1\Delta H$, however we tend to observe otherwise, due to finite modulation.

positive solution of ω_{res} increases, leading to higher H_0. As $\Gamma \propto \omega$, so FWHM is also expected to increase. Since, $\Gamma \propto \alpha$ also, it is ideal to have higher orders of frequencies to work upon.

Chapter 2

Introduction to Experimental Components

2.1 Lock-in Amplifier

Lock-in amplifiers enable detection of extremely small AC signals (down to nanovolts) even when buried in large noise by using phase-sensitive detection, which isolates only the component of the signal at a chosen reference frequency and phase. For example, a $10nV$ signal at $10kHz$ amplified by $1000\times$ becomes $10\mu V$ but is overwhelmed by $1.6mV$ broadband noise. Even with a high-Q bandpass filter, the noise ($50\mu V$) still exceeds the signal ($10\mu V$), making accurate measurement impossible. However, using a lock-in's PSD with a very narrow detection bandwidth (e.g., $0.01Hz$), the noise drops to $0.5\mu V$ while the signal remains $10\mu V$, yielding a signal-to-noise ratio of 20 and enabling precise measurement[10].

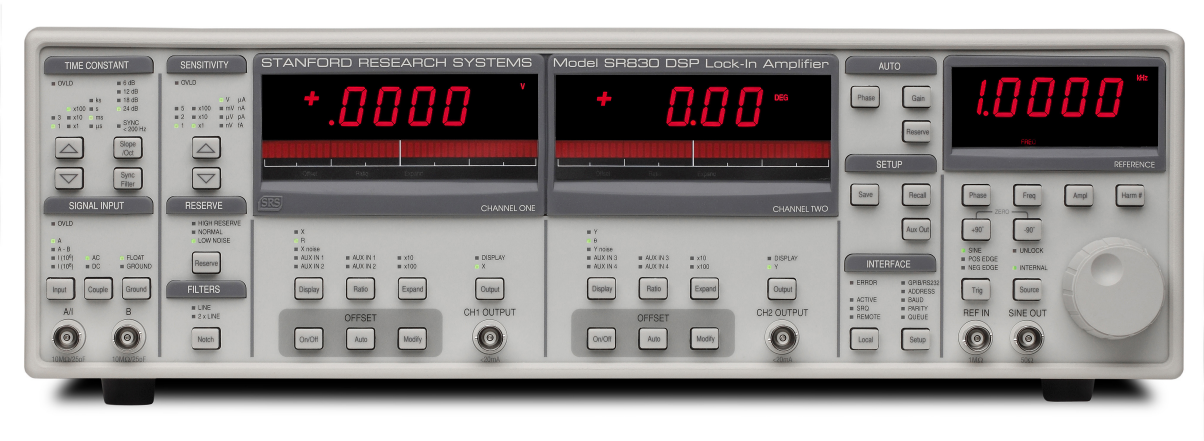

Figure 2.1: SR830 DSP Lock-in Amplifier (source:[17])

Fundamentally we take an input signal and a reference signal, be it internal or external. Then the lock-in will find the amplitude of the input signal's component, which is of the same freequency as the reference frequency. Internal signal. It does so, using a simple technique called as PSD or Phase sensitive detection.

2.1.1 Working Principle

Let the input signal be:

$$S(t) = A\cos(\omega t + \phi) + \text{noise}(t)$$

Reference signals:

$$R_X(t) = \cos(\omega t) \quad \text{(In-phase)}$$
$$R_Y(t) = \sin(\omega t) \quad \text{(Quadrature)}$$

upon multiplication (Mixing), we get the in-phase and quadrature component as:

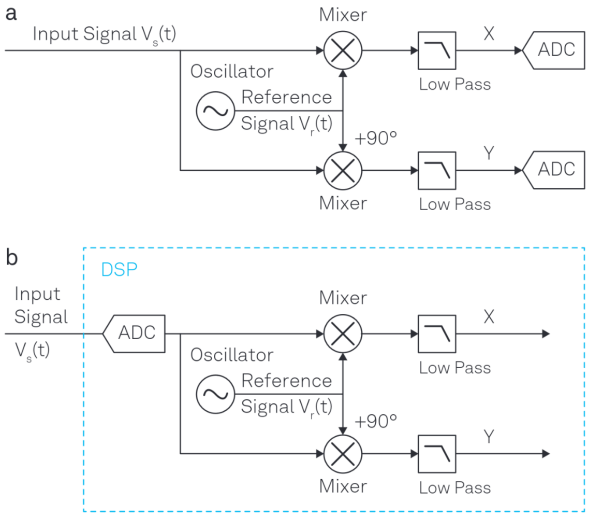

Figure 2.2: Lock-in's interal working's block diagram (source: [24]). (a) *Analog lock-in*: Signal is split, mixed with reference, filtered, then digitized. (b) *Digital lock-in*: Signal is digitized first, then multiplied and filtered digitally ***like SR830***.

In-Phase component (X-Phase):

$$S(t) \cdot R_X(t) = A\cos(\omega t + \phi) \cdot \cos(\omega t)$$

Using identity: $\cos(a)\sin(b) = \frac{1}{2}[\sin(a+b) + \sin(a-b)]$, we get:

$$= \frac{A}{2}[\cos(\phi) + \cos(2\omega t + \phi)]$$

Quadrature component (Y-Phase):

$$S(t) \cdot R_Y(t) = A\cos(\omega t + \phi) \cdot \sin(\omega t)$$

Using identity: $\cos(a)\sin(b) = \frac{1}{2}[\sin(a+b) + \sin(a-b)]$, we get:

$$= \frac{A}{2}[\sin(2\omega t + \phi) + \sin(\phi)]$$

DC terms here are kept, as they are the respective phase's component of reference frequency. After applying a **low-pass filter (LPF)**, the high-frequency terms are removed:

$$X = \text{LPF}[S(t) \cdot R_X(t)] = \frac{A}{2}\cos(\phi)$$
$$Y = \text{LPF}[S(t) \cdot R_Y(t)] = \frac{A}{2}\sin(\phi)$$

giving us:

$$\text{Amplitude:} \quad R = \sqrt{X^2 + Y^2} = \frac{A}{2} \tag{2.1}$$

$$\text{Phase:} \quad \phi = \tan^{-1}\left(\frac{Y}{X}\right) \tag{2.2}$$

2.1.2 Low-Pass Filter Equations

First-order RC filter:

$$H(\omega) = \frac{1}{1 + i\omega\tau}, \quad \tau = RC \tag{2.3}$$

which taken for nth-order (to check for further harmonics):

$$H_n(\omega) = \left(\frac{1}{1 + i\omega\tau}\right)^n$$

Slope would be $n \times 6$ dB/octave (or set slope) for each nth order, implying higher order filters would attenuate those harmonics, more aggresively. τ however, does not affect the slope, but rather the response time of the capacitor, hence setting the cutoff frequency as $f_{-3dB} = 1/(2\pi\tau)$ for $n = 1$, adjusted for higher n. So, the time constant τ basically shifts the -3db point of the filter, to start roll off early or later [24].

Filter properties considered for the settings in SR830 ($\tau = 1$):

n	Roll-Off (dB/oct)	$f_{-3\text{dB}}$	f_{NEP}	$f_{\text{NEP}}/f_{-3\text{dB}}$	63.2%	90%	99%	99.9%
1	6	0.159	0.250	1.57	1.00	2.30	4.61	6.91
2	12	0.102	0.125	1.23	2.15	3.89	6.64	9.23
3	18	0.081	0.094	1.16	3.26	5.32	8.41	11.23
4	24	0.069	0.078	1.13	4.35	6.68	10.05	13.06

Table 2.1: Filter properties for nth-order RC filters with $\tau = 1$. For same $f_{-3\text{dB}}$, τ decreases with n.

2.1.3 Minimum Settings

So if we want to get rid of 99% noise, i.e. a 1% **settling accuracy**, we need to use $\tau \times 10.05$ (n=4). Example: if we have a 1 MHz signal, then for a 1 kHz BW (n=4), $\tau = 69\ \mu s$. So for a 1% settle, it becomes 0.7 ms. A 1% Settling Accuracy implies, how closely the lockin output settles to $\pm 1\%$ of the final value after a transcient. Also note:
Phase error: $\arg[H(\omega)] = -n \arctan(\omega\tau)$;
Amplitude error: $|H(\omega)| = \frac{1}{\sqrt{1+(\omega\tau)^2}}$. so error would be $(1 - |H(\omega)|) \times 100\%$, as rest of signal is preserved. Hence, a ***high τ should also be avoided*** under certain circumstances.

2.2 Schotkky Diode based RF detector

A Schottky diode forms a junction between a metal and an n-type semiconductor. Unlike a regular p-n junction diode, it relies on the metal-semiconductor barrier to control current flow. For Forward Bias, Electrons easily cross the barrier from semiconductor to metal, resulting in low forward voltage drop (typically $\sim 0.2 - 0.3V$) and fast switching, allowing high frequency (GHz) applications.

In particular, we are going to use **BAT63–02V Infineon diode** in combination desccribed in Figure 2.3.

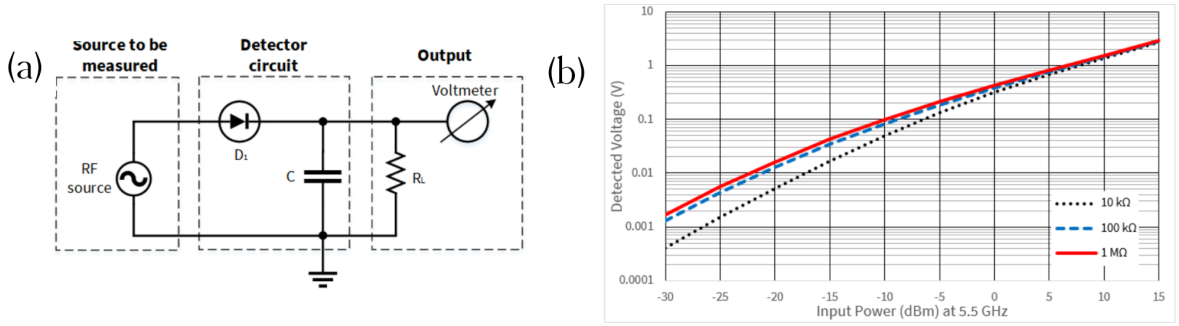

Figure 2.3: (a) Schotkky used as RF signal detector. (b) Output signal characterstics (source: [1])

Since Ideal V_{dc} for a perfect rectification should be V_{peak}/π and for no rectification, should be 0, We then say make up a number for how well it rectifies for our diode as:

$$\text{rectification metric} = 1 - |(V_{peak}/\pi - V_{dc})/V_{peak}|$$

defining how well is it rectifying at the given frequency (higher the better).

We then make a labview code, having used LF signal generator from our signal generator and getting a trace using our 500MHz oscilloscope and calculate how well, the diode behaves. Most ordinary diodes fail the test, in MHz regime, unlike Schotkky diode.

We then measure, general DC output using a simple voltmeter, and are able to recreate the graph as in Figure 2.3.

Purpose of this circuit

We aim to convert the RF signal to DC signal with amplitude proportional to RF's amplitude, while not eliminating low frequencies, hence giving the ability to detect them using lock-in, since we can not lock in with SR830 at frequencies above 102KHz. RF constant is thus chosen, keeping the same in mind, to not eliminate lower frequencies.

- **Bypass capacitor C is chosen to be 1 nF** so that it has low ohmic capacitive reactance up to 6 GHz. Hence we can not operate it above around 6GHz.
- Load resistance is chosen to be $1M\Omega$.
- Refer to [1] for details requiring the BAT63–02V Infineon diode.

NOTE: This particular Schottky fails to operate well above 6GHz when used without any bypass capacitance and load resistance, as we measure the Vrms directly using a multimeter.

2.3 Helmholtz Coils

We can use general Biot-Savart Law, from which we know:

$$d\vec{B} = \frac{\mu_0}{4\pi} \cdot \frac{I\, d\vec{l} \times \vec{r}}{|\vec{r}|^3}$$

Which, for one coil, of Radius R at a distance z, on it's axis is given by:

$$B_z = \frac{\mu_0 I}{4\pi} \int_0^{2\pi} \frac{R^2\, d\theta}{(R^2 + z^2)^{3/2}}$$

where, $\vec{r} = -R\cos\theta\,\hat{\imath} - R\sin\theta\,\hat{\jmath} + z\,\hat{k}$, and $|\vec{r}| = \sqrt{R^2 + z^2}$, and *theta* is angle between radius $\vec{r}$ pointing inwards, and $z\hat{k}$.

Upon solving which and superimposing for both coils, at a distance d from each other ($z = d/2$ for both), general formula for the magnetic field at the midpoint between two identical coaxial circular coils becomes:

$$\boxed{B_{\text{center}} = \frac{\mu_0 N I R^2}{\left(R^2 + \frac{d^2}{4}\right)^{3/2}}} \tag{2.4}$$

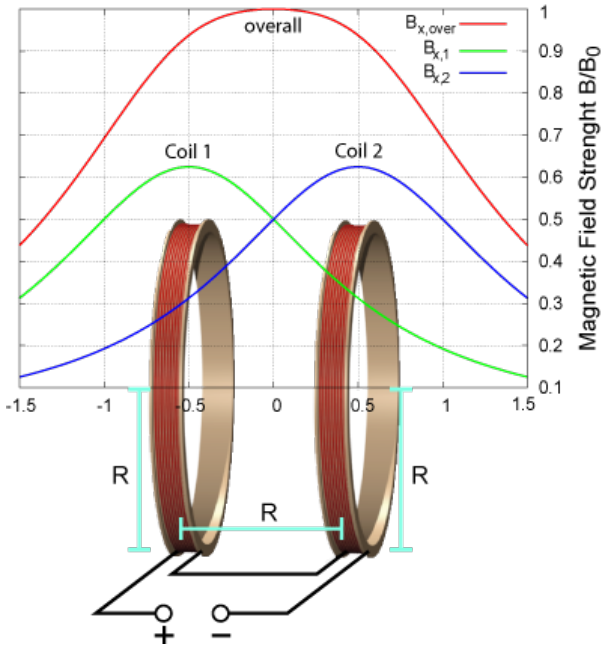

Figure 2.4: Helmholtz Coil's AC in space magnetic field, which should be taken care of while doing FMR. (source: virtuelle-experimente.de)

Hence, it is not hard to see, why coil placement must be as ridgid as possible, and also, how placing a gaussmeter at a different position than sample, would lead to different result, which should be precalibrated experimentally, by placing the gauss probe (used to record B at every point in FMR) at same position as the sample, and then taking a similar set of readings, by placing it slightly above the sample, in range of Magnetic Field of interest. Notice, the calibrated difference is not supposed to be constant, since magnetic field difference between two points is dependent of the current through coils.

2.4 Coplanar Waveguide and Impedance Matching with BNC

2.4.1 Calculating CPW Impedance

A coplanar waveguide is a planar transmission line where the signal conductor and the two ground conductors lie on the same surface of a dielectric substrate. The signal strip is separated from the grounds by narrow slots. We will keep our sample on top of the transmission line to allow microwave to pass through the surface of the sample. Most of the electric field is concentrated in the slots between the center strip and the grounds, with some fringing into the air above. The magnetic field loops around the center conductor, confined mostly in the slot regions. This current produces an oscillating magnetic field H_{rf} in the slot regions, with a strong in-plane component right above the gaps. The oscillating field couples to the sample's magnetization $\boldsymbol{M}$, acting as the driving torque in the Landau-Lifshitz-Gilbert (LLG) equation.

Note that sample thickness interacting is limited by microwave skin depth (typically $\sim 1-10\mu m$ at GHz frequencies) i.e. microwave travels only at the surface in contact with the CPW[3].

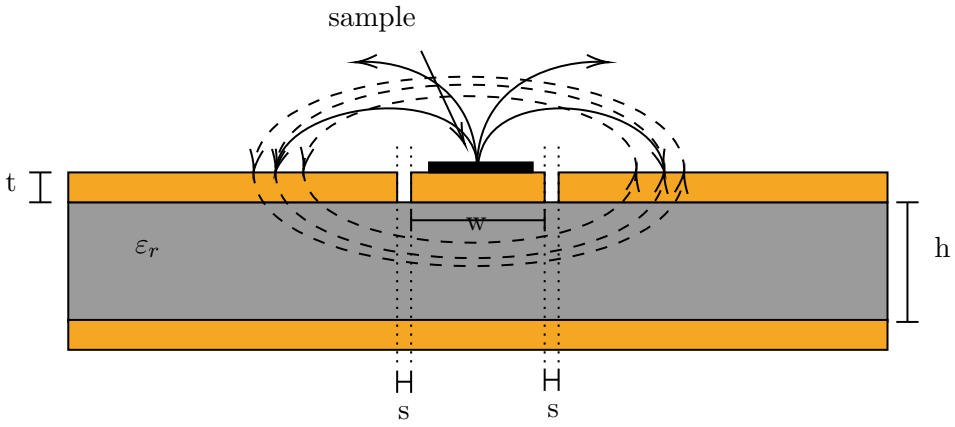

Figure 2.5: Coplanar Waveguide Side view.

Using the equation 3.8.3 in [16], We have used PVC board with copper, hence $\varepsilon_r \approx 3.2$. Assuming it is thick enough, we can say $h \geq 3w$. The copper layer, at the top and bottom of PVC can be assumed to have, $t \ll ht$. Estimate the Effective Permittivity ε_e as:

$$\varepsilon_e \approx \frac{\varepsilon_r + 1}{2} \approx \frac{3.2 + 1}{2} = 2.1.$$

Since ground plate at the bottom of PVC is also covering full area, we can call it approximately an ideal CPW. THen we can define the elliptic modulus k as:

$$k = \frac{w}{w + 2s} \tag{2.5}$$

with w being the stripe width, and s being the gap between strip and each ground plate.

$$Z_0 = \frac{30\pi}{\sqrt{\varepsilon_e}} \frac{K'(k)}{K(k)}, \tag{2.6}$$

i.e eqn 3.8.3 [16], Where $K(k)$ and $K'(k) = K(\sqrt{1-k^2})$ are complete elliptic integrals approximately given by eqn 3.8.5 and 3.8.6 [16] as:

$$\frac{K'(k)}{K(k)} \approx \begin{cases} \dfrac{\ln\left[2\,(1+\sqrt{k})/(1-\sqrt{k})\right]}{\pi} & 0 \leq k \leq 0.707, \\ \dfrac{\pi}{\ln\left[2\,(1+\sqrt{k})/(1-\sqrt{k})\right]} & 0.707 < k < 1. \end{cases} \tag{2.7}$$

2.4.2 50Ω Impedance Matching

coplanar waveguide (CPW) behaves as a transmission line with some characteristic impedance Z_0, which depends on its geometry and substrate. Common coaxial cables (like BNC cables) are designed with $Z_0 \approx 50\Omega$. If the impedance is not matched at the signal transitions between the BNC cable and the CPW, part of the wave will be reflected at the interface instead of being fully transmitted with reflection coefficient:

$$\Gamma = \frac{Z_{line} - Z_0}{Z_{line} + Z_0}.$$

Hence, putting $Z_0 = 50\Omega$ in Equation 2.6 and combining with Equation 2.7, we get,

$$\frac{K'(k)}{K(k)} = \frac{Z_0\sqrt{\varepsilon_e}}{30\pi} = \frac{50\sqrt{2.1}}{30\pi} \approx 0.75$$

$$\ln\frac{2(1+\sqrt{k})}{1-\sqrt{k}} = 0.75\pi \implies \sqrt{k} \approx 0.81 \implies k \approx 0.65$$

$$k = \frac{w}{w+2s} = 0.65 \implies \boxed{\frac{w}{s} \approx 3.7}$$

giving us the ratio between strip width and gap between them as 3.7. There are plenty of online calculators which are better at such calculations, with alot more parameters, kept in mind, that one may use. A VNA (Vector network analyser) would be a good idea to use, if available, to directly calculate impedance.

2.5 Bias Tee

A microwave RF bias-tee is a three-port network that merges DC and RF signals onto a single 50Ω line (or splits them apart) by exploiting the frequency-selective reactances of an inductor and a capacitor. At RF frequencies the inductor behaves as an open, while at DC it's a short; the capacitor is a short at RF and an open at DC [15]. Denoting the operating angular frequency $\omega = 2\pi f$, the two key impedances are

$$Z_L = j\,\omega\,L, \quad Z_C = \frac{1}{j\,\omega\,C}.$$

for a properly working bias tee, one requires:

$$Z_L(\omega_{\mathrm{RF}})| \gg Z_0, \quad |Z_C(\omega_{\mathrm{RF}})| \ll Z_0,$$

so that at f_{RF} the DC port (through L) is effectively open and the RF port (through C) is effectively a direct pass. The common port is able to see only the $50ohm$ system impedance over the GHz band, yielding negligible reflection. Impedance matching around GHz therefore reduces to choosing:

$$L \gg \frac{Z_0}{\omega_{\mathrm{RF}}}, \qquad C \gg \frac{1}{\omega_{\mathrm{RF}}\,Z_0}.$$

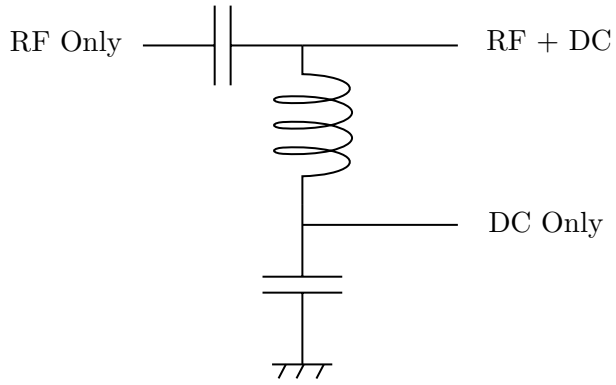

Figure 2.6: Basic bias tee circuit for RF/DC signal separation

Chapter 3

Setup

3.1 Spectrum Analyser Based FMR

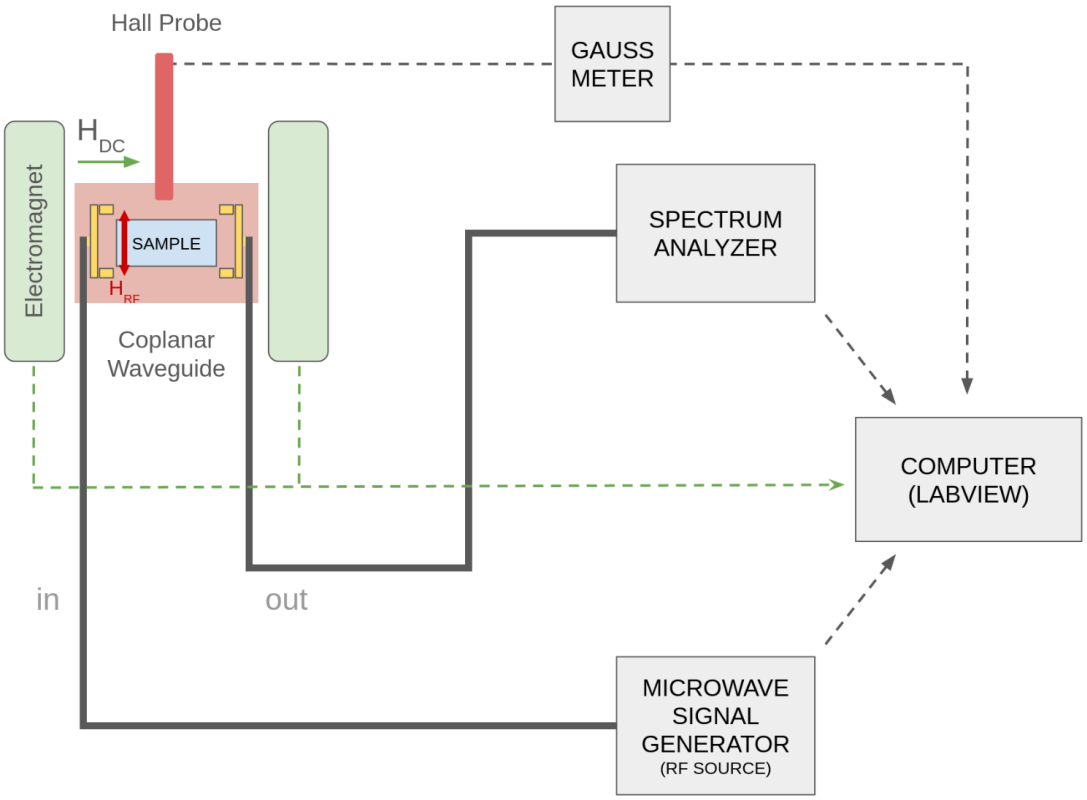

Figure 3.1: FMR using Spectrum Analyser general Overview.

- The sample is kept on the waveguide. A DC magnetic field is applied on the sample along the long axis and face down on the waveguide. RF at 5.5GHz is provided and received through the R&S Spectrum Rider FPH.
- Output is set to 6dBm at 5.5GHz through R&S SMB100A RF port. This corresponds to 2.9dBm at the waveguide and -0.2dBm at the spectrum analyser as per cable power loss as discussed in the next section (read precautions section first point).

- Current is provided to the Electromagnet to set the DC Magnetic field (H_{DC}).
- A sample is provided with the RF (in direction of H_{DC}, hence making the H_{RF} perpendicular to H_{DC}).
- Spectrum Analyser then picks up the amplitude of the frequency's peak and amplitude through the inbuilt set marker position feature.
- H_{DC} vs RF received amplitude is plotted and we expect to see a lorentzian absorption peak around the H_{DC} corresponding to resonance.

3.2 Lock-in Amplifier Based FMR

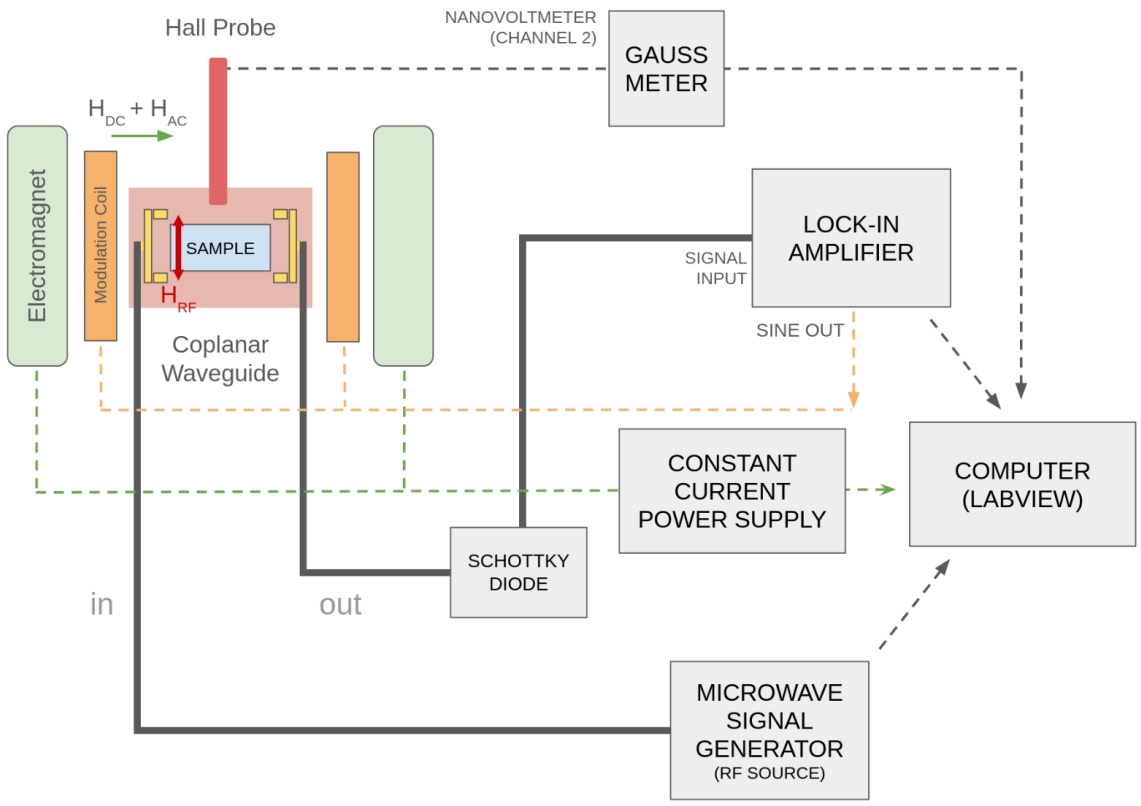

Figure 3.2: FMR using Lock-in Amplifier general Overview.

The setup is fundamentally similar to the one used in the Spectrum Analyser case, with both measurement modes applicable here as well. Key differences and operational details are outlined below:

- **RF Source:** A continuous RF signal is sent at **9.7 dBm** and **5.5 GHz**.
- **Modulation Coils:** Two modulation coils are directly affixed to the cores or body of the electromagnet. This configuration aims to generate an alternating magnetic field (H_{AC}) perpendicular to the static field (H_{DC}). See Figure 3.3.
- **AC Field Generation:** Current is supplied to both coils in the same direction (clockwise), producing H_{AC}. This current is modulated as a sine wave using the reference output of the lock-in amplifier.

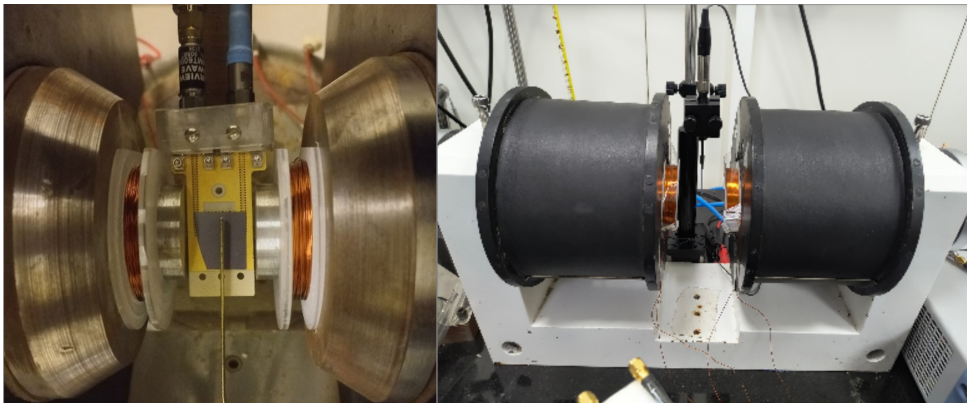

Figure 3.3: Helmholtz coil / modulation coil configuration — shown on the left (source: Magnetic Lab @ AUB) and in our lab on the right.

- **Reference Frequency:** Set to approximately **80 Hz**, chosen to avoid harmonics of power line frequencies (50/60 Hz).
- **Field Modulation Principle:** A strong static magnetic field (H_{DC}) is swept, while a small oscillating field (H_{AC}) is superimposed. Near resonance, this modulation causes the RF absorption to vary slightly, resulting in amplitude modulation of the RF signal at the same frequency as H_{AC}.
- **Detection Mechanism:**
  - A Schottky diode rectifies the RF signal, converting amplitude fluctuations into a voltage signal.
  - The resulting voltage contains a small AC component at the modulation frequency.
  - This AC component is extracted by a lock-in amplifier tuned to the reference frequency, isolating the signal from background noise and DC offsets.
- **Signal Interpretation:** The lock-in output is proportional to the slope of the absorption curve at each point in the H_{DC} sweep, enhancing resonance detection sensitivity.
- **Phase Adjustment:** The lock-in's X (in-phase) component typically exhibits a sine-wave-like response. The lock-in phase must be adjusted to account for the phase difference between the reference sine wave and the actual H_{AC} received.

3.3 Nanovoltmeter Based FMR

- The setup is similar to the Spectrum Analyzer case, with the key difference being the detection method for RF amplitude.
- Instead of using a spectrum analyzer, a Schottky diode is employed to rectify the RF signal and convert it into a DC voltage.
- The DC output from the Schottky diode is directly proportional to the amplitude of the RF signal, providing the desired measurement quantity.
- A nanovoltmeter is used to measure this DC voltage, allowing detection of amplitude variations near the resonance region.
- A bias tee is introduced to eliminate any residual AC component from the RF signal before it reaches the nanovoltmeter, preventing potential damage to the equipment.

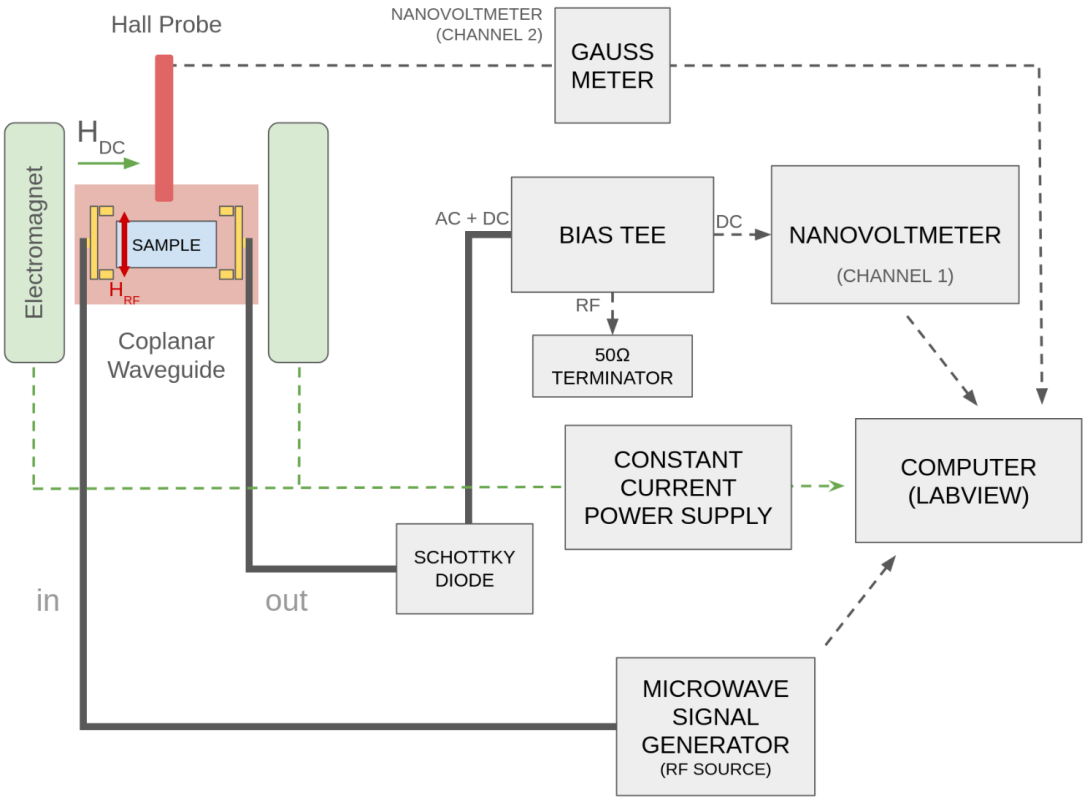

Figure 3.4: FMR using Nanovoltmeter general Overview.

- The RF signal is terminated after the Schottky diode, and only the DC component is extracted for measurement.
- A similar absorption peak is expected as in the spectrum analyzer case, corresponding to resonance-induced changes in RF amplitude.

3.4 Setting Up Components

3.4.1 Electromagnet Description

Currently the Hall probe and current supply to coils are controlled by the Holmarc Constant Current supply unit. It also has a temperature sensor built into the coil connected via Coil 1 wire. See Figure 3.5

3.4.2 BNC Cables and Connectors Power Loss

A BNC cable is a coaxial cable with a bayonet-style connector used for transmitting RF signals. It ensures secure, low-loss connections in lab setups, oscilloscopes, and communication systems. The central conductor carries the signal, while the outer shield blocks interference, maintaining consistent impedance, typically 50Ω for clean signal flow. However we do infact notice loss in our BNC as in Figure 3.6 and Table 3.1. The loss increases as the frequency increase, and follow power law emperically. This may be explained using skinn effect, that at higher frequencies, current flows only near the surface of the conductor. This reduces the effective cross-sectional area, increasing resistance and hence conduction loss. The skin depth δ scales as:

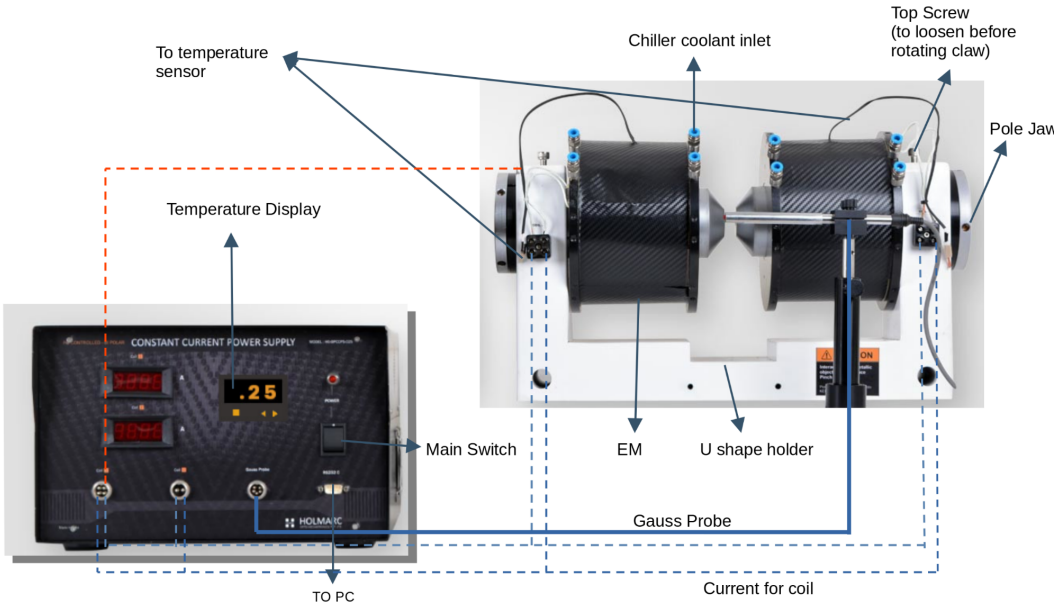

Figure 3.5: Holmarc CCSU with its wiring and unit description.

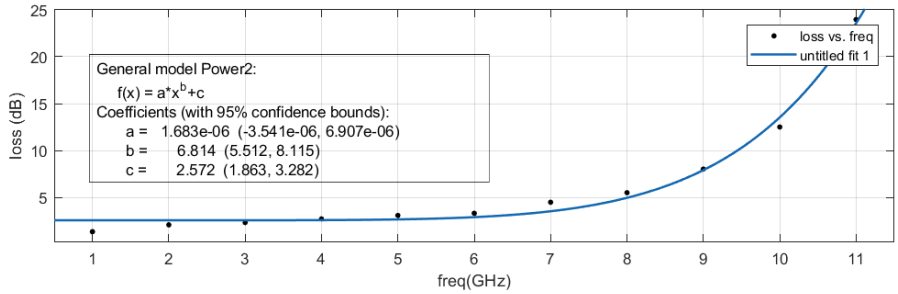

Figure 3.6: BNC cable + connector pair loss vs frquency for our setup, fit with power law.

$$\delta \propto \frac{1}{\sqrt{f}}$$

it may also be explained by dielectric loss to insulating material at higher frequencies.

Freq (GHz)	1	2	3	4	5	6	7	8	9	10
Loss (dB)	1.36	2.09	2.33	2.72	3.09	3.32	4.50	5.51	8.03	12.51

Table 3.1: Measured insertion loss of BNC cable across RF frequencies for reference.

3.4.3 Modulation coils for our setup and measuring B using Lock-in

Purpose of modulation coil is to produce H_{AC}, as discussed in section 1.5. Hence, we input into it, a reference frequency via signal generator/lockin output. Since, current provided is AC, as per Equation 2.4, B would also be AC.

- Resistance: $\sim 7\Omega$ each, i.e. 3.5Ω combined in parallel.
- This output is received by our coils with combined resistance of 3.5Ω receives a current of 150mA rms, i.e $\sim 1.5v$ by calculation as well as in Oscilloscope

- Upon passing 1.5V DC through both the coils in parallel, B received 0.83mT DC.
- When using the lock-in amplifier at a low frequency of 0.1Hz, we notice that the gauss probe in H_{DC} mode registers 1.5mT peak to peak.
- From the previous point, if we directly input the gauss probe output to lock-in signal input, we notice, 1.5mT corresponds to 0.13mV in gauss probe output 'R' reading.
- Then increasing it to 80Hz results in 0.09mV in gauss probe output 'R'. This can be interpolated to 0.95mT peak to peak oscillation of H_{AC} at 80Hz from lock-in sine out at 5V.

This way, we have been able to map output B at our operating 80Hz frequency of the coils, using lock-in amplifier, combined with direct gauss probe output. Shape of the output can also be traced by differing the reference frequency from the coil's frequency by, small amout $\sim 0.05Hz$, and plot the in-phase component in labview.

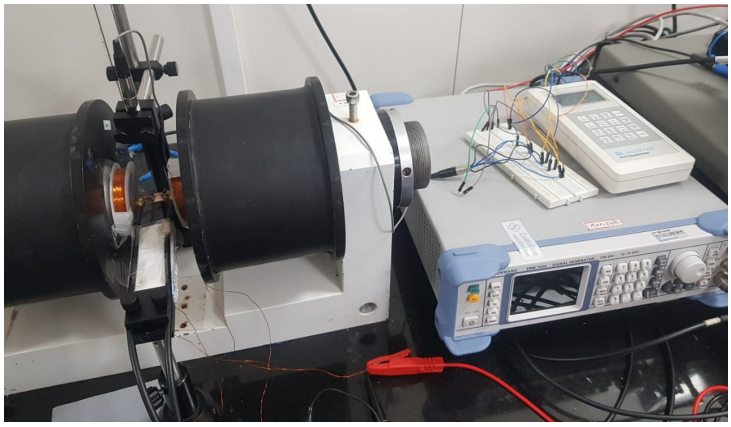

Figure 3.7: Placement of sample on CPW in Electromagnet between Modulation coils.

Kindly note we have used coils in Parallel in our case, however, a series connection might be better since resistance adds up and is better accepted by lock-in as a load due to higher impedance, and, would also ensure equal current flowing through both coils.

3.4.4 Lockin Settings

Lockin settings currently used are as follows:

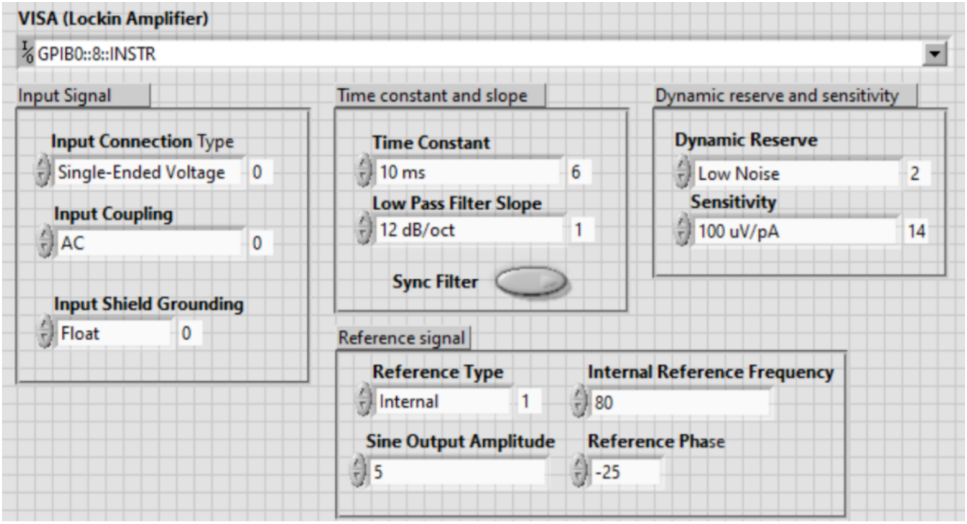

Choice of the settings justified as follows:

- Input connection type is put to Single ended Voltage since we are using only single input A.
- Coupling is there to reject the DC component as it would not be reflected by the lockin.
- Input Shielding is chosen to float because:
  - Cleaner signal, especially for low-level AC measurements, as experienced.
  - Avoid baseline noise floor which was coming on using ground mode creating a DC offset.
  - minimize EMI coupling and ground loops.
- Time constant is chosen such that it should be greater than $\tau = 1/(2\pi f_{\min})$ and hence, anything greater than 1.989ms should be fine for 80Hz. As a rule of thumb, output settles to 99% of final value in about $5 \times \tau$. Hence it is chosen as 10ms
- Low pass filter slope is chosen as standard 12db/oct as we are currently not concerned with speed/responsiveness, but rather care more about noise rejection.
- Sync filter is not turned on since our output is jittery, however, it might be better to use if we are sure we are modulating a signal with a clean reference, i.e modulation is confirmed to give a clean sine H_{AC}.
- Low noise Dynamic reserve is chosen assuming signal, when once received is not buried under noise. However, it might be better to use High Reserve for better noise attenuation.
- Reference signal is chosen to be 80Hz internal as discussed already and Sine output corresponds to 5V (rms) i.e. 14.14V peak to peak, given high impedance load as per the manual for SR830 and as measured using the multimeter when no load.
- Reference phase is decided from the output of gauss probe when put into lockin and theta provided. We are assuming this is completely the phase due to induction of the coils as can be calculated using $\boldsymbol{\phi = \tan^{-1}(\omega L/R)}$. This hopefully restores the signal to phase component X completely. One may however not apply this phase and still expect residual signals to appear in the Y component. Ideally, One may use **Autophase** button on lockin while they are at a known B with sample, on, where the FWHM of sample exists, i.e a peak exists.

3.5 Precautions and Notes

3.5.1 Precautions

- **Never** let **FPH Spectrum Rider** ever receive **more than 0dBm input**. Leads to instrument failure. Verify the same using per cable dB loss whenever exceeding 0dBm from the signal generator. Check the section for per cable loss in this pdf.
- Ensure the modulation coils are behaving correctly using the oscilloscope to measure the voltage across them. Leads to unexpected results very often. Prefer to use the probe that came with the R&S oscilloscope directly instead of connecting via a BNC cable to avoid reflections.
- Do not let the temperature exceed 40^oC in the Electromagnet coils. Keep the Chiller and Holmarc CCSU unit on and connected to keep a check on the same, if using setup B and no alternate to measure temperature is there.

- Use Bias tee as a filter to clear out any rf component before measuring the DC using nanovoltmeter.
- Clean the Waveguide using IPA before each use. Use Vinegar for etching Oxide layer on Waveguide. Handle samples with care and vacuum desiccate when not in use.

3.5.2 Notes

- Always run the instruments for 10 minutes as warmup before final measurements.
- Keep in mind that each T connector splits the incoming wave's voltage into half for the 2 outgoing waves given impedance matches.
- Make sure every single part of circuit, including the oscilloscope (if any), waveguide and Schottky diode are all **50Ω impedance** as, are the BNC cables, since any form of impedance mismatch results in power loss due to reflection. Oscilloscope should be set to 50Ω impedance when used with BNC.
- Lots of wires and cables and connectors are faulty. Please check loose or faulty connections before concluding.
- Make sure the sample is well magnetized.

3.6 Alternate Setups and Labview Codes *(Lab Specific)*

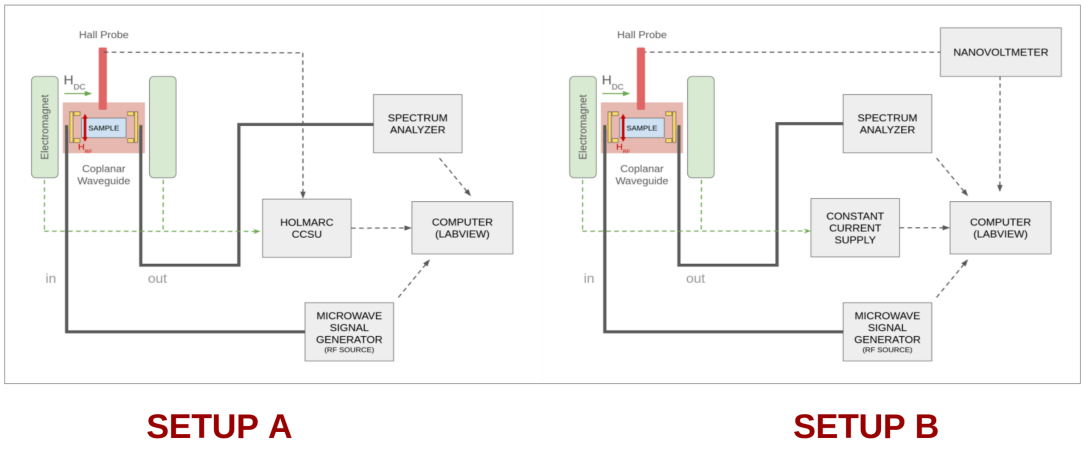

Figure 3.8: Variants of the setup using both Holmarc CCSU done earlier and the Using the R&S Constant Current Supply for the coils and Keithley nanovoltmeter for checking the Magnetic field directly with a lot more precision on the right side to achieve 0.1mT precision.

Core idea being removal of the Holmarc Constant Current Supply Unit (Setup A) due to its slow and inaccuracy in setting the significant digits of Current. Hence, we instead use setup B as follows:

- **R&S Power Supply NGL202**: Used as a constant current source on Channel 1.
- **Keithley Nanovoltmeter 2182**: Employed for Gauss probe measurements. The Gauss probe from Lakeshore can be connected directly, and the voltage across the respective ports measured using the nanovoltmeter to determine the magnetic field B, as per the precalibrated values. Kindly refer to *Shiva_Folder* for calibration details. For the current source, we continue using the Gaussmeter itself by tapping the respective wires from the probe.

- **Arduino-based Thermistor Measurement**: The thermistor embedded in the coils is directly connected to the Arduino. A known resistance is placed in series across the A0 pin, ground, and 5V supply. Refer to *Sarthak_Folder* for the implementation details.

3.6.1 Labview Codes

Closed Loop Gauss probe to EM R&S Power Supply Drivers

Mainly, with Setup B in mind, kindly find closed loop drivers made for setting Magnetic field using the R&S Power supply and the original Holmarc Gauss probe, under
`Abhay_Saxena/Power_Source_Based_Electromagnet`.
Drivers folder contains, the respective drivers that may be used directly to set the B. First import the
`set_B_hall_probe_rfs_int_stop_driver.vi`
Program to connect with both gauss probe and the power supply. Use the same program to stop the connection. Then, to run the program, kindly use the
`set_B_hall_probe_rfs_driver.vi`.

FMR using spectrum analyser

For utilizing **Setup A** (Holmarc CCSU case), the relevant codes are located under:

- `Abhay_Saxena/FMR_spectrum_analyser/FMR_Spectrum_Analyser_measure_B`: This version measures the magnetic field B using the Gauss probe during every run, alongside spectrum peak analysis.
- `Abhay_Saxena/FMR_spectrum_analyser/FMR_Spectrum_Analyser_no_B`: This variant skips the Gauss probe measurement of B during each run and focuses solely on spectrum analysis.

No combined code for setup B. Kindly use Shiva's Nanovoltmeter based Gauss probe driver, Sarthak's Temperature sensor code and given drivers in Abhay Folder for Electromagnet to combine the same and achieve 0.1mT precision. Currently codes are focused on checking for signal hence we do not use any gauss probe and roughly Change the iteration of current by 23mA from the current supply (corresponding to 0.1mT change roughly) for quick run through.

FMR using Lock-in Amplifier

Setup A: Holmarc CCSU Case:
The code for Setup A is a modified version of the original LabVIEW program found in `Piyush_Folder`. In this version:

- The **Set B drivers** have been replaced to allow finer resolution in magnetic field B.
- The setup utilizes the **Holmarc CCSU** system, as expected for Setup A.
- The LabVIEW program is located at:
  `D:/Abhay_Saxena/FMR_lock-in/FMR_Lock-in_setB/FMR_Lockin V3.vi`

Setup B: Preliminary FMR Scans:
Unlike the ideal Setup B, the current implementation does not integrate Shiva's Nanovoltmeter-based Gauss probe driver and Sarthak's Arduino-based temperature sensor. Instead:

- The code estimates magnetic field B using a general conversion factor of **0.0023 mA per 0.1 mT**, which may vary depending on the pole gap.

- Constant current is varied across predefined steps, as precise field resolution is not critical during preliminary FMR signal detection.
- The program displays all four lock-in outputs: **X, Y, R, and** θ.
- The LabVIEW program is located at:
  `D:/Abhay_Saxena/FMR_lock-in/`
  `FMR_Lock-in_current_direct_double_channel_rfs_XYRtheta/FMR_Lockin V3.vi`

FMR using Nanovoltmeter

The LabVIEW code for nanovoltmeter-based FMR measurements is located at:
`Abhay_Saxena/FMR_nanovoltmeter/FMR_nano.vi`

Note: Integration of the Gauss probe with the nanovoltmeter has not yet been implemented. Magnetic field B is therefore not measured in real-time within this version of the code.

3.7 Description of CoFeB sample

Sample under consideration for our testing purposes is CoFeB — $Co_{40}Fe_{40}B_{20}$ (Cobalt Iron Boron) 10 nm Film on Silica Substrate, deposited via magnetron sputtering.

- Substrate: Thermally grown amorphous silica (SiO_2) is used for excellent dielectric isolation.
- Saturation magnetization ($M_s \approx 1.2T$) at room temperature.
- Interfacial perpendicular or in-plane magnetic anisotropy can be engineered via post-deposition magnetic thermal annealing (MTA).
- Intrinsic Gilbert damping constant α as low as 0.005–0.01, yielding narrow FMR linewidth ($\Delta H_{pp} < 5$ Oe), which is a little problematic for FMR.
- Amorphous nature suppresses grain—boundary scattering, improving uniform precession
- Core material in spin—transfer torque magnetic random access memory (STT—MRAM) free and reference layers responsible for Non—volatile memory in smartphones, automotive electronics, and data centers.
- Enables spin—orbit torque switching when paired with heavy metal underlayers (Pt, Ta, W), also making useful for ST-FMR.

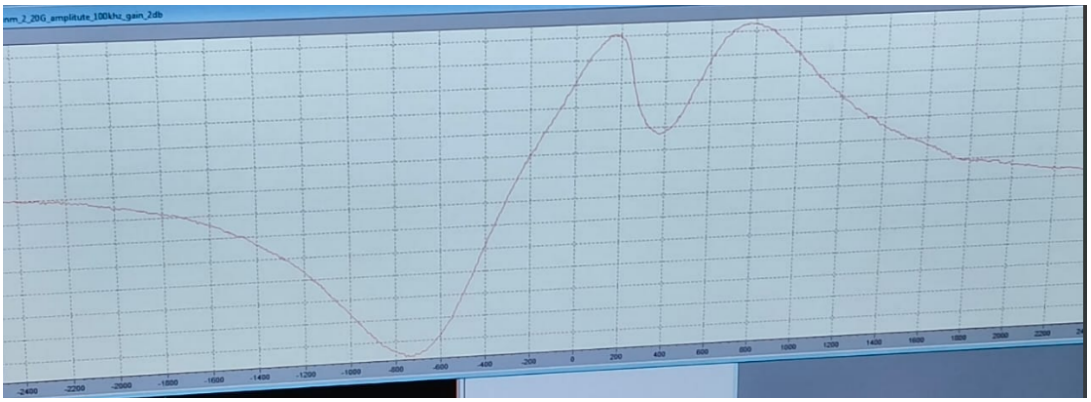

Figure 3.9: Results from EPR of CoFeB 10nm sample on Si substrate as Gauss (x-axis) vs EPR output (20 Gauss modulation at 10KHz) from IISER Bhopal central EPR facility, with a high SNR 9.45GHz cavity. Note that the dip in the secon peak is still not explained well, but most certainly accounts for the stretched teflon tape used to bind the sample to EPR rod. Given is in-phase output for direct FMR input, and out-of-phase output for Absorption Peak.

Chapter 4

Results and Discussions

4.1 Nanovoltmeter and Spectrum Analyser Based FMR

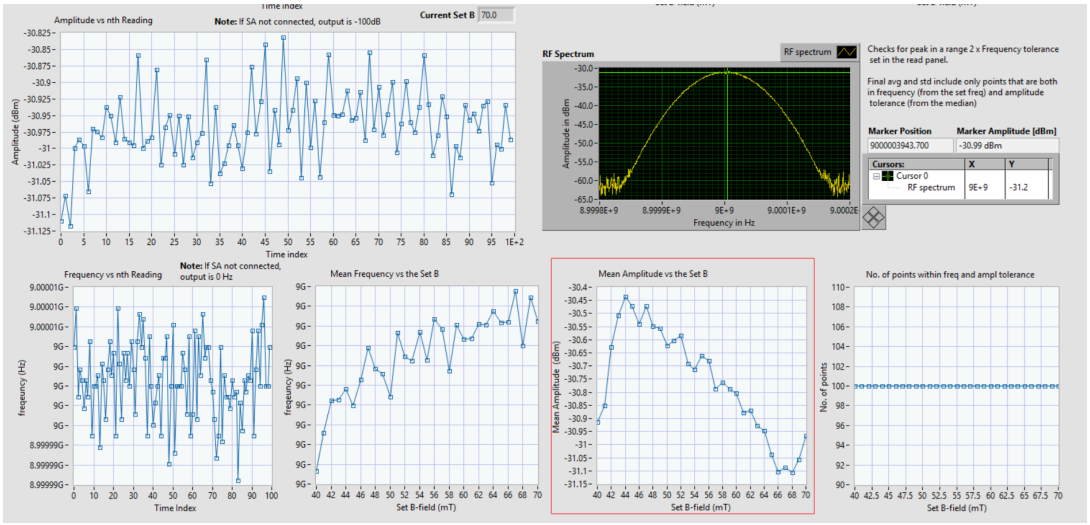

Figure 4.1: Output of Spectrum Analyser based FMR with $1/f$ drift **without** any sample, highlighted in red.

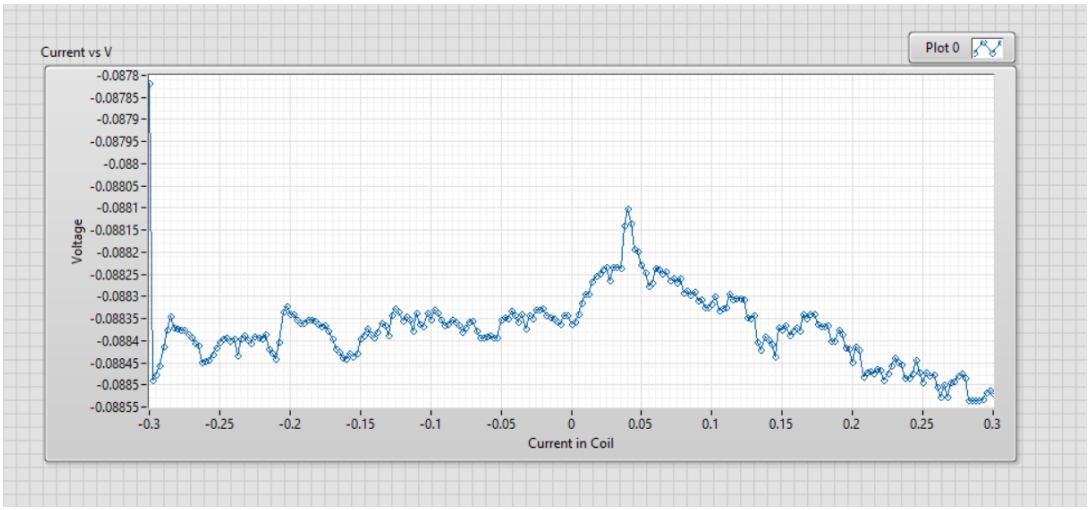

Figure 4.2: Output of Nanovoltmeter based FMR with time with sample, with noise level dips.

The output is consistantly there at these repeating cycles of very low frequency and this is one of those cycles catured in Figure 4.1. Electron drift causes the net movement of charge carriers under an applied electric field, and in solid-state components—especially semiconductors and nanostructures—this drift is modulated by scattering, mobility, and structural disorder. 1/f noise, or flicker noise, emerges from a superposition of slow, stochastic processes such as charge trapping/detrapping at interfaces, mobility fluctuations due to phonons or defects, and time-dependent variations in junction conductance, especially in percolative or thin-film systems.

4.1.1 Set vs Average B

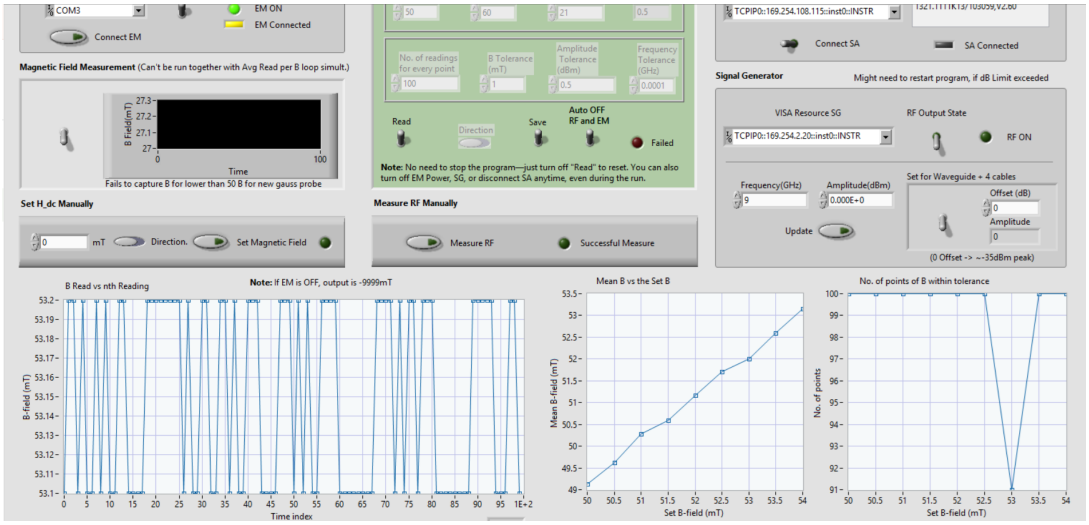

Figure 4.3: Set Current in coil, vs average B for Holmarc Constant current supply.

Set vs Average program is kept to know how well we are able to set the Magnetic field, and how well it stays constant. We then plot the average of 100 runs per set B, and plot to fint that the output is linear, in multiples of 0.5mT. However, further resokution is not achieved by Halmarc Constant current supply, and hence we instead opt for R&S constant current supply which allows us to achieve 0.1mT precision using our self written drivers.

Since the output from Spectrum amplifier tends to fluctutate alot, we instead try to average the output at a set B, since set vs average B is consistant for a particular B. For the reason we need to have a lockin Amplifier, i.e. having a chopping, to eliminate 1/f noise, we notice the same noise for the case of spectrum analyser. For the case of nanovoltmeter, however, due to lack of time, we could not verify the same.

4.2 Lock-in Amplifier Based FMR

The issue we faced in case of Spectrum Analyser is easily eliminated using a lockin amplifier, where we dont see any such drift, just some random noises points (easy to eliminate).

From Figure 4.4, it is easily visible how setting our phase has allowed us to capture all output in in-phase (X) component, and get, only noise level output in out-of-phase (Y) component. The signal in X-phase is clearly the out-of-phase output for dip in output, implying our output is shifted in phase by 180^o. This output was achieved at the frequency and lockin settings as mentioned in Figure 4.5.

If we plot the output of X-phase, from Figure 4.4, where the x-axis is not set B, but current actually, where 25mA current corresponds to 0.1mT difference and 2.36mT is core magnetization, hence an offset. This was done as an approximation, since taking gauss probe

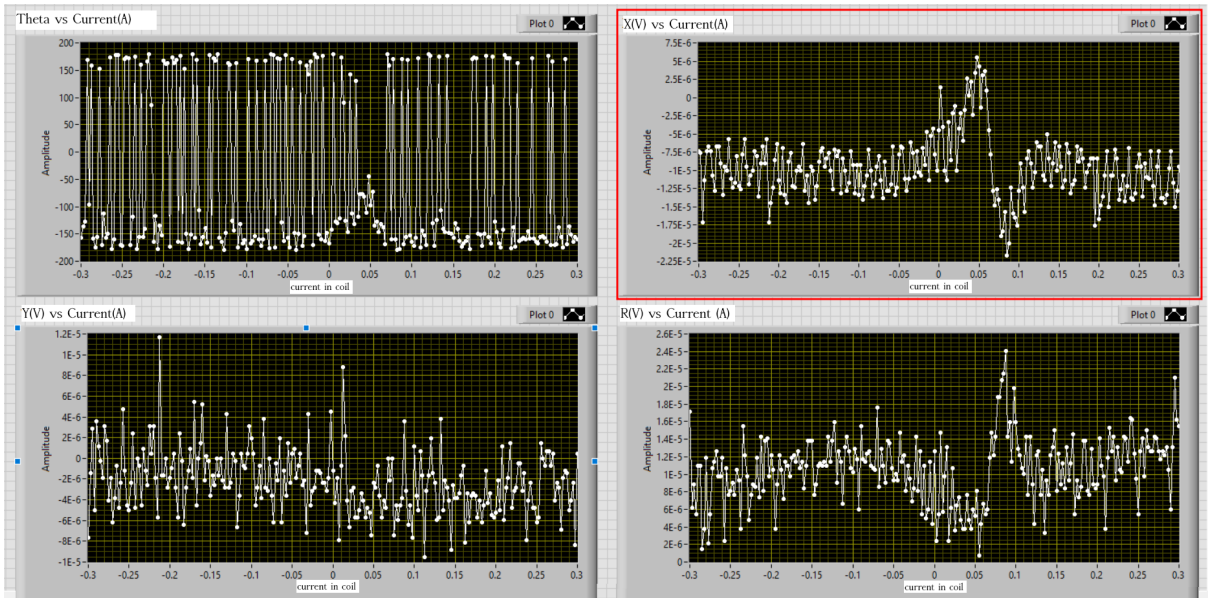

Figure 4.4: Output from lockin amplifier with CoFeB 10nm sample from all four channels X, Y R and θ components.

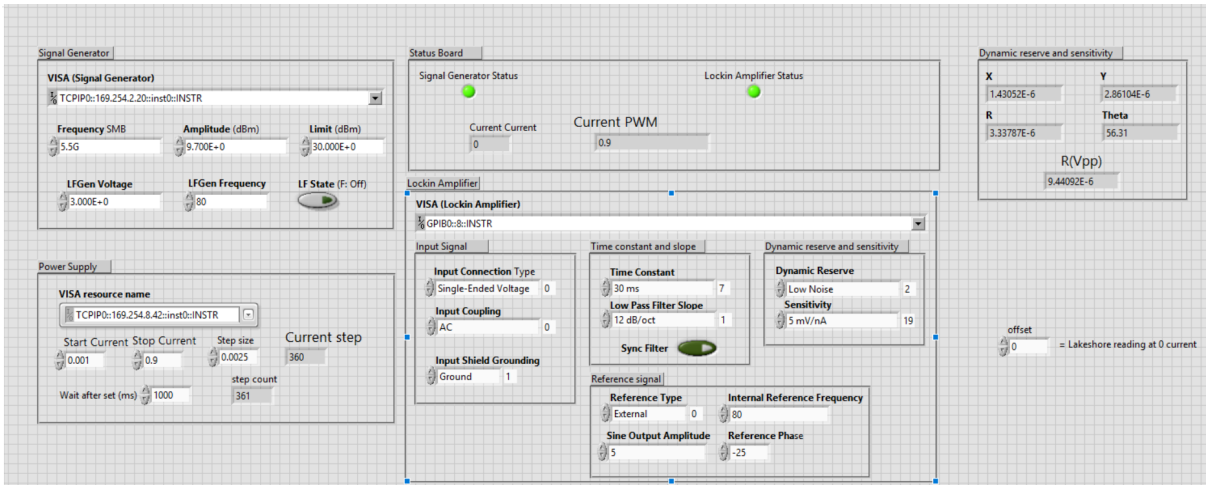

Figure 4.5: Settings used for Figure 4.4. The FMR was done at 5.5GHz with 0.5mT modulation at 80Hz.

readings every run was causing 1s delay per step and can be fixed with new nanovoltmeter based drivers for gauss probe. We fit the output with the the derivative of (1.21):

$$V_x(B) = \text{scale} \cdot \left[\frac{1}{1 + \left(\frac{B - B_0 - \delta}{\Gamma/2}\right)^2} - \frac{1}{1 + \left(\frac{B - B_0 + \delta}{\Gamma/2}\right)^2} + C \right] \tag{4.1}$$

Where, δ is the modulation amplitude (0.5mT), C is a constant baseline offset, scale is an overall amplitude scaling factor, Γ is the full-width at half-maximum (FWHM) and B_0 is the resonance peak.

The fit can be seen in Figure 4.6, where we find, $\alpha = 0.0071$ and $B_0 = 0.27$. This however, raises suspicion in validity of our output, since the B_0 is very close to B = 0, unlike for the case of ESR output with $B_0 \approx 26mT$ which is around 10 times our current B_0. We also having sweeped through region around $B = \pm 26mT$, did not find any peak.Even though we recieved no

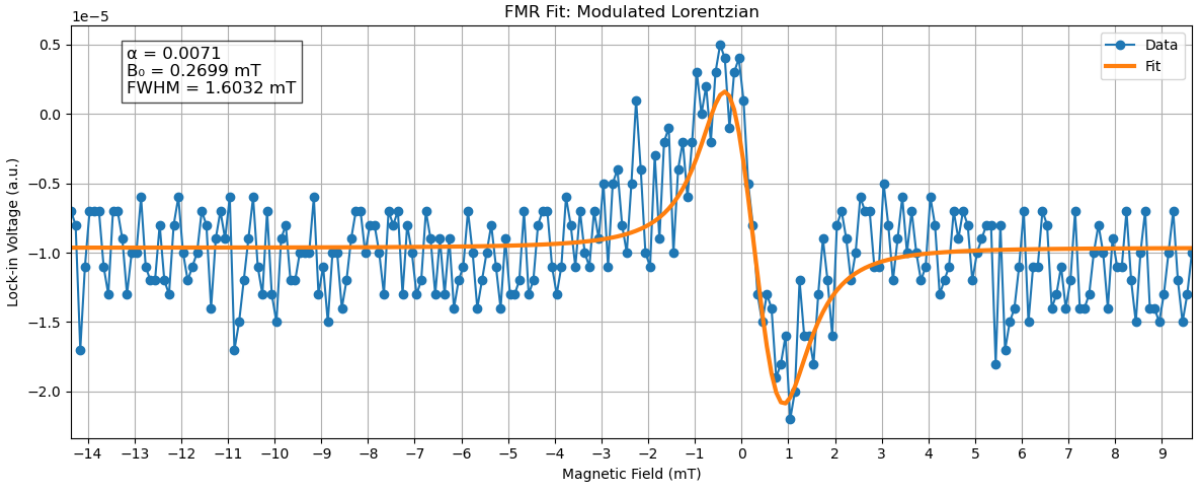

Figure 4.6: FMR output fitted with B after conversion from B to magnetic field assuming $25mA \sim 0.1mT$ and 2.36mT offset from gauss probe, measured when passing through $0mT$ point.

such signal without the sample on, from FMR, this disripancy might be due to the absorption, which results potentially from absorption of some component, at $B = 0$. It might be anything including the LCR of the Coplanar waveguide due to some deformity, or Helmholtz coils not being stuck properly and hence reacting on swtiching B, or some other reason. Or there is a problem with unit conversion from ESR output to our setup's output in mT. It is equally possible that low α of CoFeB might be a reason we are not able to find the peak at expected position due to bad least count and this is something else. Hence, even though the output looks fine, *it should not be called as FMR signal from the CoFeB sample without further investigation.*

Chapter 5

Theory of ST-FMR

Due to time constraints, only the theory of ST-FMR was covered in given time. Here we describe the working principles and ideal setup. **Most of the contents in this chapter, are based on [18] and Spintronics course lecture notes by Prof. Kuntal Roy.**

5.1 Magnetoresistance

Magnetoresistance describes how a material's electrical resistance changes under an applied magnetic field. Two common metrics are:

- Change in resistance: $\Delta R(H) = R(H) - R(0)$.
- Magnetoresistance ratio:

$$\boldsymbol{MR}(H) = \frac{R(H) - R(0)}{R(0)} \times 100\%, \tag{5.1}$$

  where $R(H)$ is the resistance in field H and $R(0)$ is the zero-field resistance.

Geometrical Magnetoresistance in semiconductor, is induced due to Lorentz force:

$$\sigma = \frac{\sigma_0}{1 + \beta\sigma_0^2 R_H^2 B^2}; \qquad \mathrm{MR}(B) = \beta \frac{R_H^2 B^2}{\rho_0^2}$$

where σ_0 is zero-field conductivity, R_H is Hall coefficient, β is the Field-dependent scattering factor. For further discussion, let's assume longitudinal direction is $\hat{x}$, the transverse direction is $\hat{y}$ and the out-of-plane direction is $\hat{z}$.

5.1.1 Anisotropic Magnetoresistance (AMR)

- AMR is the change in the resistivity of a ferromagnet depending on the angle between the electric current $\vec{J_c}$ and the magnetization $\vec{M}$.
- First observed in Fe and Ni (1850s).
- Origin is spin-orbit coupling (SOC): scattering of conduction electrons depends on the relative orientation of their spin to the magnetization direction. Hence we can say it is due to **anisotropic mixing of spin-up and spin-down** conduction bands due to spin-orbit coupling.

Longitudinal Resistivity (main equation)

The resistivity along the current direction $\hat{x}$ is:

$$\rho_{xx} = \rho_{\perp} + (\rho_{\parallel} - \rho_{\perp}) \cos^2 \phi \tag{5.2}$$

ϕ is angle between current density $\vec{J_c}$ and magnetization $\vec{M}$, $\rho_{\parallel}$ is resistivity when $\vec{M} \parallel \vec{J_c}$ and $\rho_{\perp}$ is resistivity when $\vec{M} \perp \vec{J_c}$. Note here that:

- ρ is maximum when $\vec{M} \parallel \vec{J_c} \Rightarrow \rho = \rho_{\parallel}$
- ρ is minimum when $\vec{M} \perp \vec{J_c} \Rightarrow \rho = \rho_{\perp}$

This variation is what we call as AMR. Also, since current density would be defined seperately for spin up, and down currents, $\rho^{\uparrow}(\theta) \neq \rho^{\downarrow}(\theta)$. One may measure AMR using Planar Hall effect, as discussed ahead.

5.1.2 Complete picture of Transverse Resistivity in Ferromagnets

The total transverse resistivity ρ_{xy} includes contributions from:

- **Ordinary Hall Effect (OHE)**: $R_0 H_z$
  Originates from Lorentz force acting on charge carriers in an external magnetic field H_z (out-of-plane). It is dominant in non-magnetic materials or at high fields and independent of magnetization direction.
- **Anomalous Hall Effect (AHE)**: $R_A M_z$
  Originates from Spin-orbit coupling and intrinsic band structure effects in ferromagnets. Proportional to the out-of-plane component of magnetization M_z.It is often nonlinear in M, and can dominate at low fields in magnetic materials. Discussed in section 5.2.
- **Planar Hall Effect (PHE)**: $(\rho_{\parallel} - \rho_{\perp}) \sin \phi \cos \phi$
  a phenomenon where an in-plane magnetic field generates a transverse voltage in a material, and the voltage is dependent on the angle between the magnetic field and the applied current. Arises from the angular dependence of resistivity due to symmetry of the AMR tensor as discussed in this section with Longitudinal Resitivity being the other component of AMR tensor. Depends on the in-plane angle ϕ between current and magnetization.

Combining all terms:

$$\rho_{xy} = R_0 H_z + R_A M_z + (\rho_{\parallel} - \rho_{\perp}) \sin \phi \cos \phi \tag{5.3}$$

Here, H_z is out-of-plane magnetic field, M_z is out-of-plane magnetization, ϕ is in-plane angle between current $\vec{J_c}$ and magnetization $\vec{M}$, R_0 is the Ordinary Hall coefficient and R_A is Anomalous Hall coefficient.

5.1.3 Giant Magnetoresistance (GMR)

Giant magnetoresistance (GMR) is the large change in electrical resistance of a multilayer or spin-valve structure when the relative magnetization of adjacent ferromagnetic layers switches between parallel (P) and antiparallel (AP) alignment.

$$\text{GMR} = \frac{R_{\text{AP}} - R_{\text{P}}}{R_{\text{P}}} \times 100\%, \tag{5.4}$$

Two-Current Model for CPP

We assume that the conduction electrons split into two independent channels labeled ↑ (say, majority spin) and ↓ (say, minority spin). Each channel has its own resistivity in a single ferromagnetic layer then, as $\rho^{\uparrow}$ (low scattering here) and $\rho^{\downarrow}$ (high scattering here). Layers are assumed to be perfectly spin-conserving i.e. no spin flips occur within a layer. Then resistance for parallel and anti-parallel alignments as given in Figure 5.1, for an FM/NM/FM layer (spin-valve) can be give by:

$$R_P = \frac{2R_{\downarrow\uparrow} \cdot R_{\uparrow\uparrow}}{R_{\downarrow\uparrow} + R_{\uparrow\uparrow}} \qquad R_{AP} = \frac{R_{\downarrow\uparrow} + R_{\uparrow\uparrow}}{2} \tag{5.5}$$

where, in $R_{\downarrow\uparrow}$, first arrow represents the electron spin and the second one represents magnetization direction. This can be easily shown if we assume that, even for N repetitions of F/N bilayers (F = ferromagnet, N = nonmagnet), each spin channel flows through a series of layer resistances but the two channels remain in parallel overall. Notice, that we are treating

$$R_{\downarrow\uparrow} = R_{\uparrow\downarrow}, \qquad R_{\uparrow\uparrow} = R_{\downarrow\downarrow}.$$

It is easy to notice that, for any $R_{\downarrow\uparrow} \neq R_{\uparrow\uparrow}$, R_P, R_{AP} through simple algebra. As a metric for Magnetoresistance, we define:

$$\text{GMR} = \frac{R_{AP} - R_P}{R_P} = \frac{(R_{\uparrow\uparrow} - R_{\uparrow\downarrow})^2}{4R_{\uparrow\uparrow}R_{\uparrow\downarrow}} \tag{5.6}$$

Model equally applies to CIP case, as defined ahead, however, it is not as straight forward as CPP case, and hence, is not discussed here.

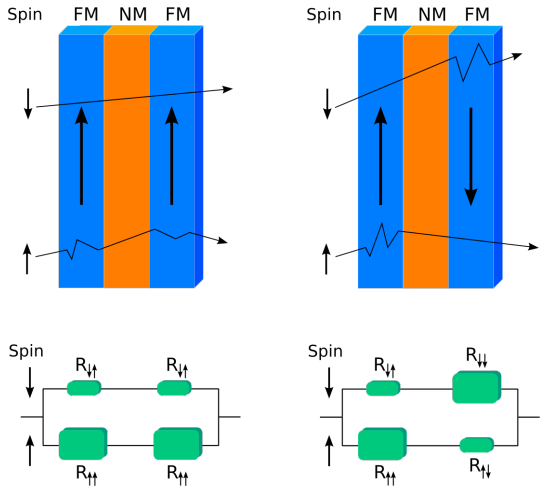

Figure 5.1: Resistor model of **spin-valve** for giant magnetoresistance effect in CPP case. FM = ferromagnetic, NM = non-magnetic (Source: Guillom. (2006) Wikimedia Commons).

Current-In-Plane (CIP) Geometry and the Boltzmann Transport Equation

In the **CIP** geometry, the applied electric current flows *parallel* to the plane of the layers in a multilayer stack. Electrons undergo numerous scattering events within the bulk of each layer and at interfaces between layers. The dominant length scale is the electron's *mean free path* λ.

The semi-classical **Boltzmann Transport Equation** (BTE) model describes the non equilibrium electron distribution function $f^{\sigma}(\vec{r}, \vec{k})$ for spin channel σ (↑ or ↓). The core equation in

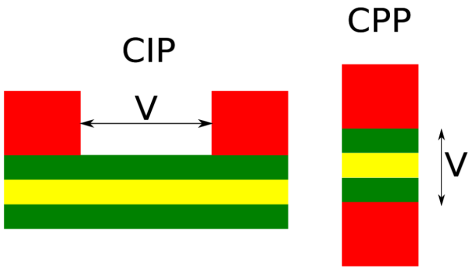

Figure 5.2: V is applied voltage between conductors (red), green and yellow: schematically ferromagnetic and non magnetic layers (Source: Alex-engraver (2011) Wikimedia Commons).

the relaxation time approximation (RTA) is:

$$\vec{v} \cdot \nabla_r f^\sigma + \frac{q}{\hbar} \vec{E} \cdot \nabla_k f^\sigma = -\frac{g^\sigma(\vec{k})}{\tau^\sigma} \tag{5.7}$$

where:

- $\vec{v}$: Electron group velocity
- f_0: Equilibrium Fermi-Dirac distribution
- $g^\sigma(\vec{k}) = f^\sigma(\vec{k}) - f_0(\epsilon_k)$: Deviation from equilibrium
- $\vec{E}$: Applied electric field
- q: Electron charge
- τ^σ: Spin-dependent relaxation time (the average time between scattering events for a spin-σ electron)

The solution to Eq. 5.7 yields the spin-dependent current density $\vec{\jmath}^\sigma$, leading to a local spin-dependent Ohm's law $\vec{\jmath}^\sigma = \sigma^\sigma \vec{E}$. The model incorporates spin-dependent bulk scattering ($1/\tau^\sigma$) and interface scattering through boundary conditions, modeling the complex in-plane transport paths in CIP geometry [23].

Current-Perpendicular-to-Plane (CPP) Geometry and the Valet-Fert Formalism

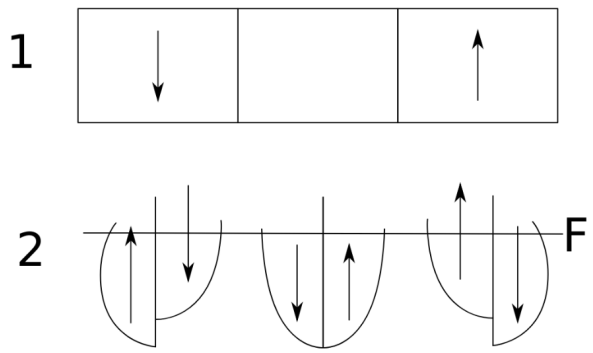

Figure 5.3: Electronic density of states (DOS) in magnetic and non-magnetic metals, for AP case, splitting for electrons with different spin directions for each layer (Source: Alex-engraver (2011) Wikimedia Commons).

In the **CPP** geometry, the current flows perpendicular to the layers as described in Figure 5.1. Every electron must cross all interfaces. The key phenomenon is *spin accumulation*, a buildup of spin polarity at interfaces, which relaxes over the *spin diffusion length* l_{sf}, the dominant length scale ($l_{sf} \gg \lambda$).

The **Valet-Fert formalism** is a macroscopic diffusive model that describes this via the spin-dependent electrochemical potential $\mu^\sigma(z)$. It consists of two coupled equations:

1. *Spin-dependent Ohm's Law:* The current density for each spin channel is driven by the gradient of its electrochemical potential.

$$j^\sigma = -\frac{\sigma^\sigma}{q}\nabla\mu^\sigma \tag{5.8}$$

2. *Continuity Equation:* The divergence of the spin current is proportional to the local spin loss due to spin-flip scattering.

$$\nabla j^\sigma = -\frac{q}{\tau_{sf}^\sigma}(\mu^\sigma - \mu^{-\sigma}) = -\frac{q}{N_F}\frac{D^\sigma}{{l_{sf}^\sigma}^2}\delta\mu \tag{5.9}$$

where:

- σ^σ: Spin-dependent conductivity
- τ_{sf}^σ: Spin-flip scattering time
- D^σ: Spin-dependent diffusion constant
- $l_{sf}^\sigma = \sqrt{D^\sigma \tau_{sf}^\sigma}$: Spin diffusion length
- N_F: Density of states at the Fermi level
- $\delta\mu = \mu^\uparrow - \mu^\downarrow$: Spin accumulation

These equations are solved for the entire multilayer stack with boundary conditions enforcing current continuity. The total resistance is found from the change in the average potential $\overline{\mu} = (\mu^\uparrow + \mu^\downarrow)/2$. This formalism is the standard model for CPP because it explicitly solves for the spin accumulation that governs the physics [20].

5.1.4 Tunneling Magnetoresistance (TMR)

If we use an insulating barrier instead of a NM conducting layer between the two FM layers, as was the case for GMR, we still end up observing magnetoresistance effect called as tunneling magnetoresistance or TMR. Recent advancements in TMR have lead to immidiate application in magnetic storage devices, especially hard disks.

One easy way to have a rough idea about TMR, would be to look at the density of states. We assume that initially, both the DOS have same Fermi energy, and upon application of an external voltage V_a, we get one level raised above the fermi energy level E_f by the eV_a. The main assumption is that the spins are conserved during the transport. Conductance of each spin direction is then, determined by the density of states for each spin as:

$$G^{\sigma_1\sigma_2} \propto N_L^{\sigma_1} N_R^{\sigma_2} \tag{5.10}$$

for σ_1 being spin of carrier and σ_2 being the magnetization of FM layer.

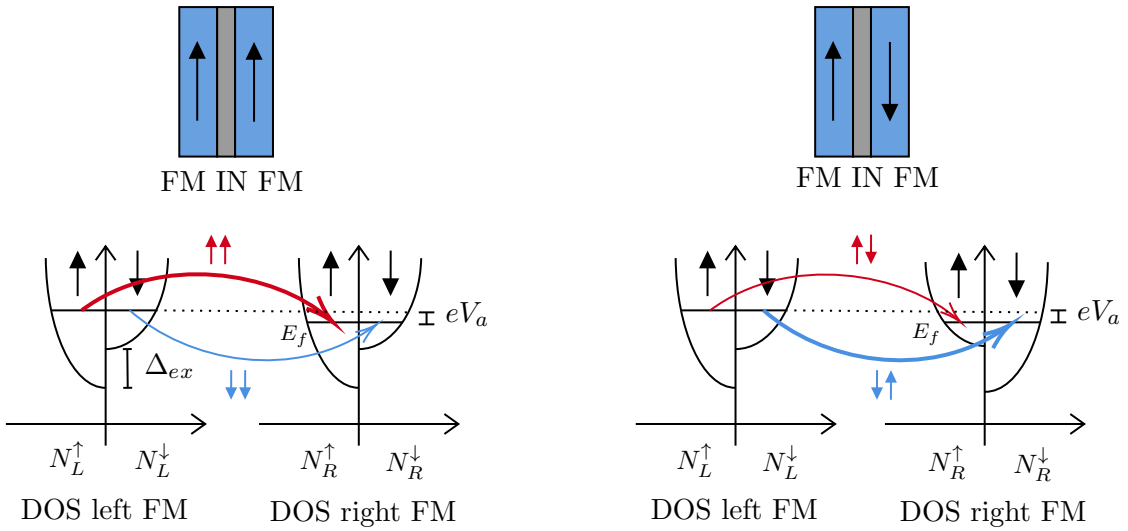

Figure 5.4: DOS demonstrating tunneling process between ferromagnetic subbands for P and AP configurations. Conduction Channels (tunneling) are shown via coloured markers with thick ones for majority (↑) carriers. The spin-resolved density of states have exchange spin splitting, Δ_{ex} (inspiration: [12]).

Notice, the Δ_{ex}, or the exchange spin splitting energy causes a gap for AP case, given the $V_a = 0$. Hence, the tunneling current is higher for parallel case, given majority carriers are ↑ for the case of Figure 5.4. TMR is then defined, just like GMR, as:

$$\text{TMR} = \frac{R_{AP} - R_P}{R_P} = \frac{G_P - G_{AP}}{G_{AP}} \tag{5.11}$$

Which, combined with (5.10), gives,

$$\text{TMR} = \frac{N_L^\uparrow N_R^\uparrow + N_L^\downarrow N_R^\downarrow - N_L^\uparrow N_R^\downarrow - N_L^\downarrow N_R^\uparrow}{N_L^\uparrow N_R^\downarrow - N_L^\downarrow N_R^\uparrow}$$

giving,

$$\text{TMR} = \frac{2P_L P_R}{1 - P_L P_R} \tag{5.12}$$

for,

$$P_i = \frac{N_i^{\sigma_1} - N_i^{\sigma_2}}{N_i^{\sigma_1} + N_i^{\sigma_2}}$$

with σ_1 being majority carrier (↑ in previous equation), and σ_2 being the minority carrier and i being the i^{th} layer L or R.

5.2 Spin and Anomalous Hall Effects

5.2.1 Spin-Orbit Coupling Fundamentals

Spin-orbit coupling (SOC) is a relativistic interaction that couples an electron's spin angular momentum to its orbital motion. This interaction arises from the magnetic field experienced by the electron in its rest frame due to the relative motion of the nucleus. SOC is fundamental to understanding various Hall effects in condensed matter systems, particularly the spin Hall effect (SHE) and anomalous Hall effect (AHE).

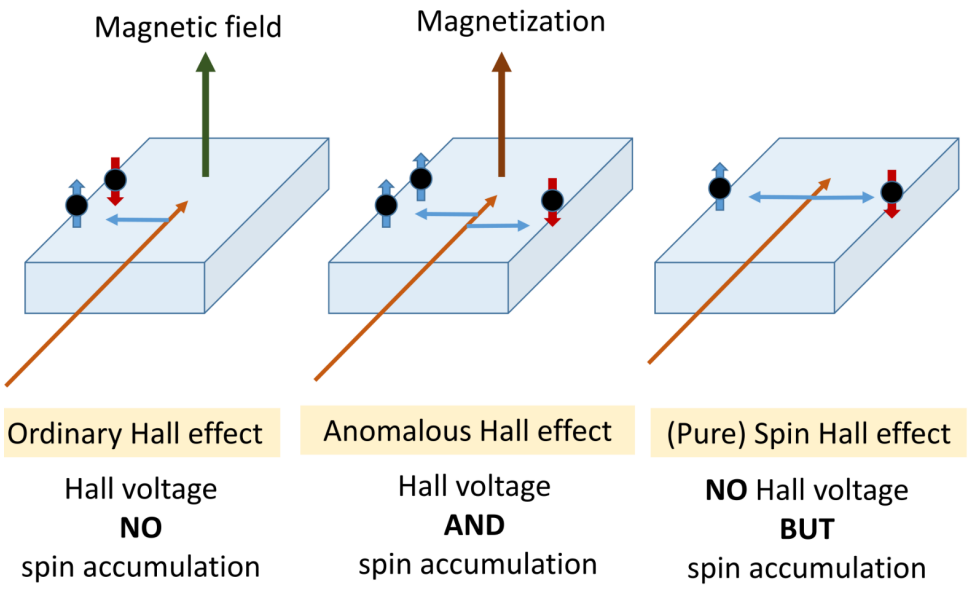

Figure 5.5: Comparing OHE, AHE and SHE (source: *lecture slides, Spintronics Course at IISER Bhopal, Dr. Kuntal Roy.*)

Atomic Spin-Orbit Coupling

For hydrogen-like atoms with nuclear charge Ze, we begin with the Coulomb potential:

$$V_{\text{int}} = -\frac{Ze^2}{r}$$

In the electron's rest frame, the nucleus appears to move with velocity $-\vec{v}$, creating a magnetic field. Using the Biot-Savart law with current element $I\vec{dl} = Ze\vec{v}$:

$$\vec{B} = \frac{\mu_0}{4\pi}\frac{Ze\vec{v}\times\vec{r}}{r^3}$$

Converting to the electric field $\vec{E} = \frac{Ze\vec{r}}{4\pi\epsilon_0 r^3}$ and using $c^2 = 1/(\mu_0\epsilon_0)$:

$$\vec{B} = -\frac{1}{c^2}\vec{v}\times\vec{E} = -\frac{Ze}{mc^2r^3}(\vec{p}\times\vec{r})$$

where we used $\vec{p} = m\vec{v}$ and $\vec{L} = \vec{r}\times\vec{p} = -\vec{p}\times\vec{r}$.

The SOC Hamiltonian arises from the interaction between the electron's magnetic moment and this field:

$$H = -\vec{\mu}\cdot\vec{B} = \frac{g}{2}\mu_B\vec{\sigma}\cdot\vec{B} \tag{5.13}$$

where $\mu_B = e\hbar/(2m)$ is the Bohr magneton and $g \approx 2$ for the electron. This gives:

$$\hat{H}_{\text{SOC}} = \frac{Ze^2}{2m^2c^2r^3}\vec{L}\cdot\vec{S} \tag{5.14}$$

Note the factor of 1/2 from the Thomas precession correction. Since $[\vec{L},\vec{S}] \neq 0$, neither L nor S are conserved. The good quantum numbers become (L^2, S^2, J^2, J_z) where $\vec{J} = \vec{L} + \vec{S}$ is the total angular momentum.

Rashba Spin-Orbit Coupling

In two-dimensional systems with structural inversion asymmetry (SIA), such as semiconductor heterostructures or surfaces, the Rashba SOC emerges. The asymmetric confining potential creates an effective electric field $\vec{E} = E_0\hat{z}$ perpendicular to the 2D plane.

Following from the relativistic transformation [2]:

$$\hat{H}_R = \alpha(\hat{z} \times \vec{k}) \cdot \vec{\sigma} \tag{5.15}$$

where the Rashba parameter α quantifies the SOC strength and depends on the electric field and material properties. The full 2D Hamiltonian becomes:

$$H = \frac{\hbar^2 k^2}{2m} + \alpha(\sigma_x k_y - \sigma_y k_x)$$

The energy dispersion exhibits spin-momentum locking:

$$E_\pm(\vec{k}) = \frac{\hbar^2 k^2}{2m} \pm \alpha|\vec{k}| \tag{5.16}$$

with helical eigenstates:

$$\Psi_{\vec{k},\pm}(\vec{r}) = e^{i\vec{k}\cdot\vec{r}} \frac{1}{\sqrt{2}} \begin{pmatrix} 1 \\ \pm e^{i\phi_k} \end{pmatrix}$$

where $\phi_k = \tan^{-1}(k_y/k_x)$ and the spin is locked perpendicular to momentum.

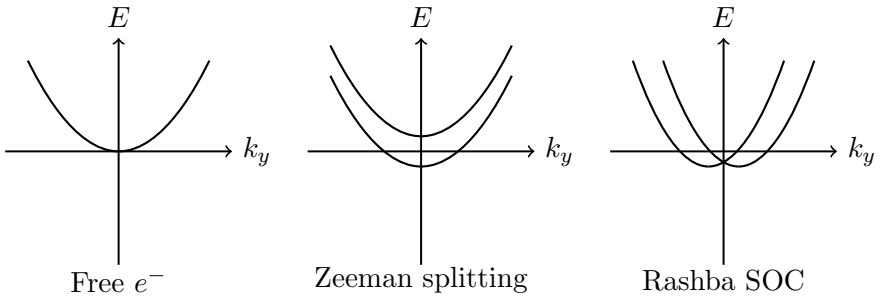

Dresselhaus Spin-Orbit Coupling

In crystals lacking bulk inversion symmetry (BIA), such as zinc-blende semiconductors, the Dresselhaus SOC emerges:

$$\hat{H}_D = \beta\left(\sigma_x k_x(k_y^2 - k_z^2) + \sigma_y k_y(k_z^2 - k_x^2) + \sigma_z k_z(k_x^2 - k_y^2)\right) \tag{5.17}$$

In quantum wells, this reduces to linear terms similar to Rashba but with different spin texture. The interplay between Rashba and Dresselhaus terms can be tuned to create persistent spin helix states important for spintronic applications.

5.2.2 Spin Current

Unlike charge current which describes the flow of electric charge, spin current represents the flow of spin angular momentum. In systems with SOC, spin is not conserved, leading to rich physics including spin relaxation and spin-charge interconversion.

The spin current density tensor describes the flow of spin component α in direction β:

$$J_s^{\alpha\beta} = \frac{\hbar}{4}\langle\{\sigma^\alpha, v^\beta\}\rangle \tag{5.18}$$

where $\{A, B\} = AB + BA$ is the anticommutator ensuring Hermiticity. For a quasi-1D system, the net spin current simplifies to:

$$J_s = \frac{\hbar}{2}(I^{\uparrow} - I^{\downarrow})$$

representing the difference between spin-up and spin-down currents.

In systems with Rashba SOC, the velocity operator acquires a spin-dependent term:

$$v_i = \frac{p_i}{m} + \frac{\alpha}{\hbar}(\hat{z} \times \vec{\sigma})_i$$

This spin-velocity coupling enables the conversion between charge and spin currents, fundamental to both SHE and spin-transfer torque phenomena.

5.2.3 Linear Response Theory and Kubo Formula

To understand the microscopic origin of Hall effects, we employ linear response theory. Consider a system described by an unperturbed Hamiltonian H_0 subjected to an electromagnetic perturbation.

For electrons in an electromagnetic field:

$$H = \frac{\left(\vec{p} - q\vec{A}\right)^2}{2m} \tag{5.19}$$

$$= \underbrace{\frac{\vec{p}^2}{2m}}_{\text{unperturbed term } (H_0)} - \underbrace{\frac{q}{2m}(\vec{p}\cdot\vec{A} + \vec{A}\cdot\vec{p})}_{\text{paramagnetic term } (H_p)} + \underbrace{\frac{q^2\vec{A}^2}{2m}}_{\text{diamagnetic term } (H_d)} \tag{5.20}$$

The diamagnetic term H_d preserves time-reversal symmetry and doesn't contribute to Hall conductivity [2]. The paramagnetic perturbation becomes:

$$\Delta H = H_p = -\vec{J}\cdot\vec{A} \tag{5.21}$$

where $\vec{J} = -e\vec{p}/m$ is the current density operator.

For an AC electric field $\vec{E} = \vec{E}_0 e^{-i\omega t}$ with $\vec{E} = -\partial\vec{A}/\partial t$:

$$\vec{A} = \frac{i\vec{E}_0}{\omega}e^{-i\omega t} \tag{5.22}$$

Using time-dependent perturbation theory in the interaction picture, the linear response of the current to the electric field gives the conductivity tensor. After considerable algebra [19], the Kubo formula for Hall conductivity emerges:

$$\sigma_{xy}(\omega) = \frac{1}{\hbar\omega}\int_0^{\infty} dt\, e^{i\omega t}\langle 0|[J_y(0), J_x(t)]|0\rangle$$

In the DC limit ($\omega \to 0$), this becomes:

$$\sigma_{xy} = \frac{i\hbar}{V}\sum_{n\neq 0}\frac{\langle 0|J_y|n\rangle\langle n|J_x|0\rangle - \langle 0|J_x|n\rangle\langle n|J_y|0\rangle}{\left(E_n - E_0\right)^2} \tag{5.23}$$

where V is the system volume and the sum runs over all excited states.

5.2.4 Topological Aspects: TKNN Formula and Chern Number

In periodic systems, the Hall conductivity can be expressed in terms of topological invariants. The Chern number, a topological invariant characterizing the global properties of Bloch bands, is defined as:

$$C_n = \frac{1}{2\pi} \int_{\text{BZ}} d^2k \, \Omega_n(\vec{k}) \tag{5.24}$$

where $\Omega_n(\vec{k})$ is the Berry curvature of band n, computed from Bloch states as described in:

$$b_n(k) = i\langle \nabla_k u_{n,k} \, | \, \times \, | \, \nabla_k u_{n,k} \rangle.$$

Using the gauge-invariant formulation with phase $\theta_n(k)$ from:

$$\overline{\Psi}_{n,k}(r) \equiv \exp(i\theta_n(k))\Psi_{n,k}(r),$$

the Chern number becomes an integral over the Brillouin zone boundary [14].

Note here that, Bloch's theorem says electrons in a crystal have wavefunctions $\Psi_{n,k}(r) = e^{ik\cdot r}u_{n,k}(r)$. The index n labels the band, k is the crystal momentum, and r is position. The cell-periodic part $u_{n,k}(r)$ changes smoothly with k. The Berry curvature $b_n(k)$ measures how $u_{n,k}$ twists in momentum space and acts like a magnetic field in k–space. The gradient ∇_k means derivative with respect to k. The phase factor $e^{i\theta_n(k)}$ shows the gauge freedom: we can multiply a Bloch state by a k–dependent phase without changing any physical result.

The celebrated TKNN formula relates the Hall conductivity to the sum of Chern numbers over occupied bands:

$$\sigma_{xy} = \frac{e^2}{h} \sum_{\text{occupied } n} C_n$$

This quantization is robust against disorder and represents a topological protection of the Hall conductance. Materials with non-zero Chern numbers in their occupied bands are termed Chern insulators.

5.2.5 Spin Hall Effect

The spin Hall effect generates a transverse pure spin current from an unpolarized charge current in nonmagnetic materials through SOC. Unlike the AHE, the SHE produces spin accumulation at sample edges without net charge separation.

Phenomenology and Spin Hall Angle

The efficiency of spin-charge conversion is characterized by the spin Hall angle:

$$\boxed{J_s^{z,y} = \frac{\hbar}{2e}\theta_{SH} J_c^x} \tag{5.25}$$

where $J_s^{z,y}$ denotes z-polarized spins flowing in the y-direction for charge current along x. Typical values range from $\theta_{SH} \sim 0.001$ in semiconductors to ~ 0.3 in heavy metals like tungsten.

Microscopic Mechanisms

The SHE arises through both intrinsic and extrinsic mechanisms:

Intrinsic mechanism: Originates from the Berry curvature of SOC-modified band structure. Using the Kubo formula for spin conductivity:

$$\sigma_{SH}^{xy} = \frac{e}{2\pi} \int_{\text{BZ}} d^2k \, f(\vec{k}) \Omega_s(\vec{k}) \tag{5.26}$$

where $\Omega_s(\vec{k})$ is the spin Berry curvature. For 2D Rashba systems, this yields a universal value:

$$\sigma_{SH}^{xy} = \frac{e}{8\pi} \text{sgn}(\alpha) \tag{5.27}$$

independent of the Rashba parameter magnitude and disorder.

Extrinsic mechanisms: Include skew scattering (asymmetric scattering from SOC) and side-jump (coordinate shift during scattering). These dominate in metals with moderate SOC.

The spin Hall angle in Rashba systems scales as:

$$\theta_{SH} \sim \frac{\alpha k_F}{E_F} \tag{5.28}$$

For Dresselhaus SOC, the spin conductivity tensor has different symmetry:

$$\sigma_{SH}^{ij} \propto \beta \epsilon_{ijk} k_k \tag{5.29}$$

Inverse Spin Hall Effect

The reciprocal process converts spin current to charge current:

$$\boxed{\vec{J}_c = \frac{2e}{\hbar} \theta_{SH} (\vec{J}_s \times \hat{s})} \tag{5.30}$$

This enables electrical detection of spin currents, crucial for experimental verification and device applications.

5.2.6 Anomalous Hall Effect

The anomalous Hall effect occurs in ferromagnetic materials, generating a transverse voltage proportional to magnetization without external magnetic field. It shares the same SOC origin as SHE but involves spin-polarized carriers.

Hall Conductivity and Mechanisms

The anomalous Hall current follows:

$$\vec{J}_c = \sigma_{xy}^{\text{AHE}} (\hat{M} \times \vec{E}) \tag{5.31}$$

where $\hat{M}$ is the magnetization direction. The anomalous Hall angle quantifies the effect:

$$\boxed{\theta_{\text{AHE}} = \frac{\sigma_{xy}^{\text{AHE}}}{\sigma_{xx}}} \tag{5.32}$$

Three mechanisms contribute to AHE, as illustrated in Figure 5.6:

Intrinsic contribution: Arises from Berry curvature of exchange-split bands:

$$\sigma_{xy}^{\text{int}} = -\frac{e^2}{\hbar} \int_{\text{BZ}} \frac{d^3k}{(2\pi)^3} f(\vec{k}) \Omega_n^z(\vec{k}) \tag{5.33}$$

The Berry curvature for magnetic systems:

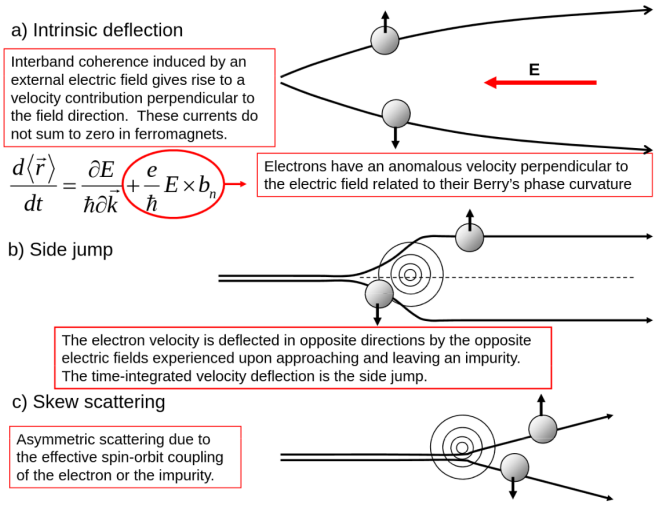

Figure 5.6: Illustration of the three main mechanisms that can give rise to an AHE. All mechanisms affect electrons in any real material (source: [9]).

$$\Omega_n^z(\vec{k}) = -2\mathrm{Im}\sum_{m\neq n}\frac{\langle n|\hat{v}_x|m\rangle\langle m|\hat{v}_y|n\rangle}{(E_n - E_m)^2} \tag{5.34}$$

Extrinsic contributions: Skew scattering and side-jump, similar to SHE but for spin-polarized carriers.

Material Dependence

In magnetic systems with Rashba SOC:

$$\hat{H} = \frac{\vec{p}^2}{2m} + \alpha(\hat{z}\times\vec{k})\cdot\vec{\sigma} + J_{\mathrm{ex}}\vec{M}\cdot\vec{\sigma} \tag{5.35}$$

The AHE conductivity scales as:

$$\sigma_{xy}^{\mathrm{AHE}} \propto \frac{\alpha J_{\mathrm{ex}} M}{(E_F - E_{\mathrm{ex}})^2} \tag{5.36}$$

demonstrating the interplay between SOC strength α and exchange splitting E_{ex}.

Typical materials exhibit: Fe ($\theta_{\mathrm{AHE}} \sim 1\%$), Co-based Heuslers ($\sim 10\%$), and magnetic Weyl semimetals ($> 20\%$). The enhancement in topological materials arises from Berry curvature singularities near Weyl points, representing the extreme limit of intrinsic AHE physics.

5.3 Spin Pumping

Spin pumping is the phenomenon where, precessing magnetization in FM layer causes spin current to flow into adjacent NM layer. As a result of this momentum transfer into the NM layer, magnetization precession is damped in the FM, resulting in larger α_{eff}. The spins are actually generated at the interface itself and then decay according to the spin diffusion length of the NM layer, λ_N. A schematic of the same along with explanation can be seen in Figure 5.7. Caption of the same discusses, how we can detect spin current using the ISHE, which generates an electrical signal from this spin current with AC component along the y direction and DC

along the x direction, i.e. the cross product direction as per (5.30). Note that this process requires:

- A strong microwave or radiofrequency drive to sustain steady precession.
- A clean FM/NM interface where electrons can exchange spin angular momentum.
- An external magnetic field to tilt and hold the magnetization at a constant cone angle θ.

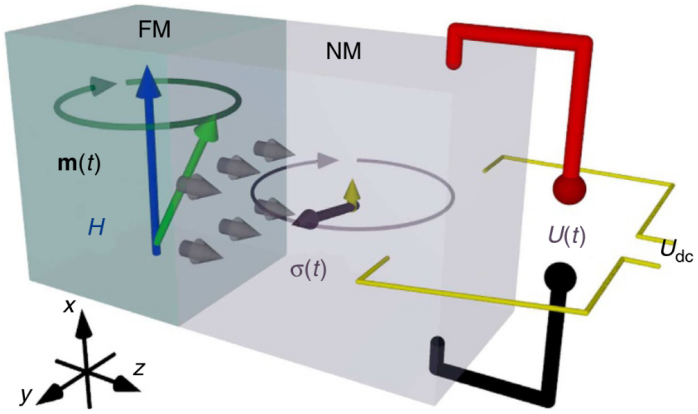

Figure 5.7: A spin current is induced at the ferromagnet-nonmagnet (FM-NM) interface through spin pumping (shown by grey arrows). The spin polarization of this current varies with time and predominantly precesses within the y-z plane (represented by the purple arrow). A small, time-averaged direct current (DC) component emerges along the x-axis (yellow arrow). Owing to the inverse spin Hall effect, both the oscillating and static spin components generate transverse charge currents in the NM layer. These can be detected as alternating current (AC) and DC voltages by placing electrical contacts along the y and x directions, respectively (source: [21]).

5.3.1 Added Damping in LLG for Spin Pumping

As already discussed, we see that the FM layer transfers momentum to NM layer resulting in a larger damping α_{eff}. Also note, that depending on the properties of the adjacent material (e.g., its ability to absorb or reflect the spin current), can lead to a shift in the observed resonant frequency or field. This is as if the LLG equation has been modified to:

$$\frac{d\vec{m}}{dt} = -\gamma_{eff}\vec{m} \times \vec{H}_{eff} + \alpha_{eff}\vec{m} \times \frac{d\vec{m}}{dt} \tag{5.37}$$

where, we find that for effective spin mixing conductance, $g_{eff}^{\uparrow\downarrow} = g_{r,eff}^{\uparrow\downarrow} + ig_{i,eff}^{\uparrow\downarrow}$ (effective, to account for spin backflow into the FM layer due to the finite NM layer, reducing the spin pumping), we can write these new effective damping and gamma terms as:

$$\frac{\gamma}{\gamma_{eff}} = 1 - \frac{\hbar\gamma}{(4\pi M_s)t_{mag}} g_{i,eff}^{\uparrow\downarrow}; \quad \alpha_{eff} = \alpha + \frac{\hbar\gamma}{(4\pi M_s)t_{mag}} g_{r,eff}^{\uparrow\downarrow} \tag{5.38}$$

Basically, this results in a shifted FMR peak, along with increased FWHM. Since we already know from (1.23), that $\alpha \propto \Delta H$ (FWHM), it is easy to see that:

$$g_{r,eff}^{\uparrow\downarrow} = \frac{(4\pi M_s)2\gamma t_{NM}}{g\mu_B\omega}(\Delta H_{\mathrm{FM\,+\,NM}} - \Delta H_{\mathrm{FM}}) \tag{5.39}$$

i.e. we can find the spin mixing conductance by comparing the output experimentally, from the modified spin pumping case's FMR's difference from the original FMR.

5.3.2 Spin Current Equation

The fundamental expression for the instantaneous spin current pumped across the FM/NM interface is given by:

$$\vec{J}_s = \frac{\hbar}{4\pi} g_{r,eff}^{\uparrow\downarrow} \vec{m} \times \frac{d\vec{m}}{dt} + \frac{\hbar}{4\pi} g_{i,eff}^{\uparrow\downarrow} \frac{d\vec{m}}{dt} \tag{5.40}$$

This equation tells us that the spin current has two components:

- The first term $\vec{m} \times \frac{d\vec{m}}{dt}$ represents the reactive (out-of-phase) component, proportional to the real part of the mixing conductance $g_{r,eff}^{\uparrow\downarrow}$. This term is always perpendicular to both the magnetization and its time derivative.
- The second term $\frac{d\vec{m}}{dt}$ represents the dissipative (in-phase) component, proportional to the imaginary part $g_{i,eff}^{\uparrow\downarrow}$.

Spherical Coordinate Transformation

To understand the temporal behavior of spin pumping, we need to express the magnetization in spherical coordinates. For a magnetization precessing around the z-axis with cone angle θ and azimuthal angle $\phi(t)$:

$$\vec{m} = \sin\theta\cos\phi\hat{e}_x + \sin\theta\sin\phi\hat{e}_y + \cos\theta\hat{e}_z \tag{5.41}$$

The time derivative becomes:

$$\frac{d\vec{m}}{dt} = \sin\theta\frac{d\phi}{dt}(-\sin\phi\hat{e}_x + \cos\phi\hat{e}_y) = \sin\theta\frac{d\phi}{dt}\hat{e}_\phi \tag{5.42}$$

where $\hat{e}_\phi = -\sin\phi\hat{e}_x + \cos\phi\hat{e}_y$ is the azimuthal unit vector.
For the cross product term:

$$\vec{m} \times \frac{d\vec{m}}{dt} = (\sin\theta\cos\phi\hat{e}_x + \sin\theta\sin\phi\hat{e}_y + \cos\theta\hat{e}_z) \times \sin\theta\frac{d\phi}{dt}\hat{e}_\phi$$

Since $\hat{e}_x \times \hat{e}_\phi = \cos\phi\hat{e}_z$, $\hat{e}_y \times \hat{e}_\phi = \sin\phi\hat{e}_z$, and $\hat{e}_z \times \hat{e}_\phi = -\hat{e}_r$, we get:

$$\vec{m} \times \frac{d\vec{m}}{dt} = \sin\theta\frac{d\phi}{dt}\hat{e}_r \times \sin\theta\frac{d\phi}{dt}\hat{e}_\phi = \sin^2\theta\left(\frac{d\phi}{dt}\right)\hat{e}_r$$

Substituting back into the spin current equation:

$$\vec{J}_s = \frac{\hbar}{4\pi} g_{r,eff}^{\uparrow\downarrow} \sin\theta\frac{d\phi}{dt}\hat{e}_r + \frac{\hbar}{4\pi} g_{i,eff}^{\uparrow\downarrow} \sin\theta\frac{d\phi}{dt}\hat{e}_\phi \tag{5.43}$$

Time-Averaged DC Spin Current

For steady precession at frequency $\omega = d\phi/dt$, the time-averaged spin current in the radial direction (which survives the time averaging) is:

$$\langle J_{s,z}\rangle = \frac{\hbar}{4\pi} g_{r,eff}^{\uparrow\downarrow} \sin\theta\omega\cos\theta = \frac{\hbar\omega}{4\pi} g_{r,eff}^{\uparrow\downarrow} \frac{\sin 2\theta}{2}$$

Converting to charge current density (multiplying by $2e/\hbar$):

$$J_{s,dc} = \frac{2e}{\hbar}\langle J_{s,z}\rangle = \frac{2e}{4\pi} g_{r,eff}^{\uparrow\downarrow} \omega \frac{\sin 2\theta}{2}$$

The DC spin pumping voltage across the NM layer is:

$$V_{SP}^{dc} = \frac{\hbar\omega}{2e}\frac{\sin 2\theta}{2}$$

And the total DC spin pumping current through a strip of width w and length l:

$$I_{SP}^{dc} = G_{SP}^{eff} V_{SP}^{dc}$$

where the effective spin pumping conductance is:

$$G_{SP}^{eff} = lw \frac{2e^2}{h} g_{r,eff}^{\uparrow\downarrow}$$

Combining these:

$$I_{SP}^{dc} = G_{SP}^{eff} \frac{\hbar\omega}{2e} \frac{\sin 2\theta}{2} = \frac{\tilde{S}\hbar\omega}{2e} G_{SP}^{eff} \sin^2\theta \tag{5.44}$$

5.3.3 Elliptical Precession Correction

In real thin film systems, magnetization precession is not perfectly circular due to strong demagnetization fields. This ellipticity must be accounted for through a correction factor $\tilde{S}$. For elliptical precession, the relationship between the measured DC spin current and the ideal circular case is:

$$J_{s,dc}^{elliptical} = \tilde{S} J_{s,dc}^{circ}$$

The ellipticity correction factor is given by:

$$\tilde{S} = \frac{2\omega(4\pi M_s\gamma) + (4\pi M_s)^2\gamma^2 + 4\omega^2}{(4\pi M_s)^2\gamma^2 + 4\omega^2} \tag{5.45}$$

This factor accounts for the fact that the in-plane and out-of-plane precession amplitudes are different due to demagnetization effects, leading to an elliptical rather than circular trajectory.

The final expression for the DC spin pumping voltage including ellipticity correction becomes:

$$V_{SP}^{dc} = \tilde{S} \frac{\hbar\omega}{2e} \sin^2\theta \tag{5.46}$$

5.4 Spin Transfer Torque and Magnetization Switching

Spin Transfer Torque (STT) is an opposite effect to spin pumping, where, from spin-polarized current, the magnetization of an FM experiences a torque due to the change in spin-angular momentum carried by the electrons. It was predicted in 1996 by Slonczewski and Berger, independently. This mechanism enables electrical control of magnetic states in nanoscale devices, forming the basis for applications such as magnetic random access memory (MRAM). The fundamental principle of spin transfer torque arises from the conservation of angular momentum. When a spin-polarized current passes through a magnetic material, the spin angular momentum is transferred from the conducting electrons to the local magnetization. Let the spin-polarization η of an electric current be:

$$\eta = \frac{I_\uparrow - I_\downarrow}{I_\uparrow + I_\downarrow} \tag{5.47}$$

with $I_\uparrow$ being current carried by spin-up electrons. Note that $1 > \eta > -1$. Also Let's define spin current magnitude be:

$$\vec{s} = \frac{\hbar}{2e} I. \tag{5.48}$$

where the factor $\frac{\hbar}{2e}$ converts electrical current to spin angular momentum current. The the Spin transfer torque (STT) exerted by spin on the magnetization of FM is:

$$\vec{\tau}_{STT} = \vec{s} \times (\hat{\eta} \times \hat{M}) \sin\theta \tag{5.49}$$

where, $\hat{\eta}$ and $\hat{M}$ are unit vectors along spin-polarization and magnetization, respectively, and θ is the angle between them. $\sin\theta$ ensures maximum torque when spins are perpendicular to magnetization. The double cross product $(\hat{n}_s \times \hat{n}_m)$ gives the direction perpendicular to both spin and magnetization, and the final cross product with $\vec{s}$ (spin current) produces the torque direction. Hence we may modify LLG to account for STT as:

$$\frac{d\vec{m}}{dt} - \alpha\vec{m} \times \frac{d\vec{m}}{dt} = -\frac{\gamma}{M}\vec{M} \times \vec{H}_{eff} = -\frac{\gamma}{M}\vec{\tau}_{STT} \tag{5.50}$$

The STT term $\vec{\tau}_{STT}$ appears on the right side as an additional torque.

5.4.1 Shape Anisotropy in STT Devices

Shape anisotropy, arising from magnetostatic self-energy, dominates the energy landscape in nanoscale STT devices and directly controls the critical switching current. The shape anisotropy energy is:

$$E_{shape}(\theta, \phi) = \frac{1}{2}\mu_0 M_s^2 \Omega N_d(\theta, \phi) \tag{5.51}$$

where the orientation-dependent demagnetization factor is:

$$N_d(\theta, \phi) = N_{d-xx}\sin^2\theta\cos^2\phi + N_{d-yy}\sin^2\theta\sin^2\phi + N_{d-zz}\cos^2\theta \tag{5.52}$$

with the constraint $N_{d-xx} + N_{d-yy} + N_{d-zz} = 1$.

The key anisotropy fields governing STT switching are:

$$H_k = (N_{d-yy} - N_{d-zz})M_s, \quad H_d = (N_{d-xx} - N_{d-yy})M_s \tag{5.53}$$

where H_k controls out-of-plane preference and H_d controls in-plane preference. For circular cross-sections ($N_{d-xx} = N_{d-yy}$), the energy simplifies to:

$$E_{shape}(\theta) = \frac{1}{2}\mu_0 M_s H_k \Omega \sin^2\theta \tag{5.54}$$

eliminating in-plane anisotropy ($H_d = 0$).

The critical switching current scales with effective anisotropy:

$$I_c = \frac{2eM_s t\alpha}{\hbar P} H_{eff} \tag{5.55}$$

where t is free layer thickness, α is Gilbert damping, P is spin polarization efficiency, and H_{eff} includes all anisotropy contributions. This direct relationship makes geometric shape engineering essential for STT optimization.

5.4.2 Spherical Coordinate Framework for Magnetization Switching

Since magnetization magnitude is conserved ($|\vec{M}| = M_s$), STT switching dynamics occur on the unit sphere surface, making spherical coordinates optimal for analysis. The unit magnetization vector is:

$$\vec{m} = \sin\theta\cos\phi\hat{e}_x + \sin\theta\sin\phi\hat{e}_y + \cos\theta\hat{e}_z \tag{5.56}$$

where $\theta \in [0, \pi]$ is the polar angle from +z axis and $\phi \in [0, 2\pi]$ is the azimuthal angle. The time derivative becomes:

$$\frac{d\vec{m}}{dt} = \frac{d\theta}{dt}\hat{e}_\theta + \sin\theta\frac{d\phi}{dt}\hat{e}_\phi \tag{5.57}$$

with the $\sin\theta$ factor ensuring proper spherical geometry normalization.

The Gilbert damping term transforms to:

$$\alpha\vec{m} \times \frac{d\vec{m}}{dt} = \alpha\frac{d\theta}{dt}\hat{e}_\phi - \alpha\sin\theta\frac{d\phi}{dt}\hat{e}_\theta \tag{5.58}$$

always opposing magnetization motion and causing energy dissipation.

For STT calculations with spin polarization $\vec{n}_s = \sin\xi\hat{e}_y + \cos\xi\hat{e}_z$, the torque components are:

$$\tau_{STT,\theta} = -s\sin\theta\cos\phi[\sin\theta\sin\phi\sin\xi + \cos\theta\cos\xi] \tag{5.59}$$

$$\tau_{STT,\phi} = s[\cos\theta(\cos\theta\sin\xi - \sin\theta\sin\phi\cos\xi) + \sin^2\theta\cos^2\phi\sin\xi] \tag{5.60}$$

where s is the spin current magnitude. The complete LLG system becomes:

$$\frac{d\theta}{dt} + \alpha\sin\theta\frac{d\phi}{dt} = -\frac{\gamma}{M}\tau_\theta \tag{5.61}$$

$$\sin\theta\frac{d\phi}{dt} - \alpha\frac{d\theta}{dt} = -\frac{\gamma}{M}\tau_\phi \tag{5.62}$$

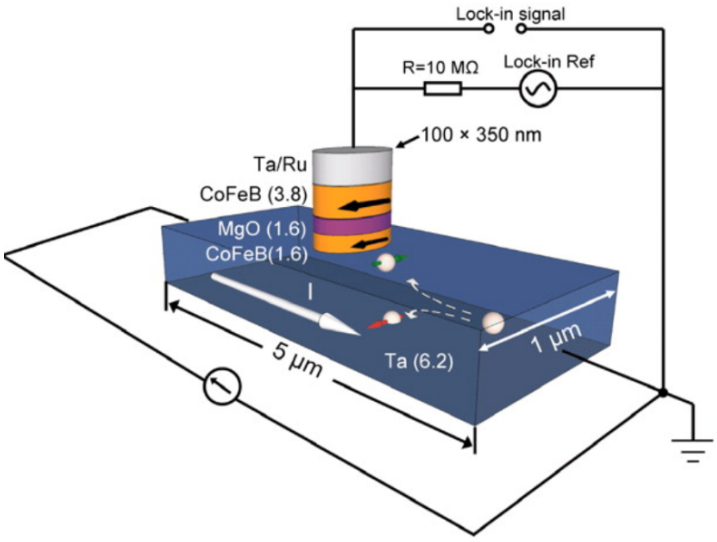

Figure 5.8: Example of STT device: 3 Terminal MTJ (Magnetic Tunnel junction), integrated with a SOT geometry. The MTJ stack consists of a MgO barrier between two CoFeB layers: the reference layer (pinned by Ta/Ru) and the free layer whose magnetization can be switched. A current perpendicular to the plane (CPP) flows through the MTJ to read its state via TMR, i.e. low resistance when magnetizations are parallel, high when antiparallel. For switching, an in-plane current is applied through the underlying Ta strip, which generates a transverse spin current via the SHE. This spin current exerts a torque on the free layer, enabling magnetization reversal between parallel and antiparallel states. Thus, the in-plane current enables SOT-driven switching, while the perpendicular current provides resistive readout, with the lock-in detection circuit enhancing signal sensitivity. (Source: [8])

Spin Orbit Torque (SOT)

Spin–orbit torque (SOT) is When an in-plane charge current flows in a heavy metal (like Ta, Pt, or W), strong spin-orbit coupling (e.g., via the spin Hall effect) generates a transverse spin current. These spins accumulate at the interface with an adjacent ferromagnet and exert a torque on its magnetization, enabling switching. Importantly, the write current flows in-plane, separate from the MTJ stack.

Difference from spin-transfer torque (STT): In STT, the write current flows perpendicularly through the MTJ, and spin-polarized electrons directly transfer angular momentum to the free layer. In SOT, the spin current is generated in the heavy metal and injected laterally, giving faster, more reliable switching with separate read/write paths. See Figure 5.8, for better understanding.

5.5 Fitting Parameters for ST-FMR

5.5.1 Basic Understanding of ST-FMR

Spin-Torque Ferromagnetic Resonance (ST-FMR) is an experimental technique that exploits the interplay between spin currents and magnetization dynamics to recreate FMR-like output. The core principle involves using an RF current to simultaneously:

1. **Drive magnetic oscillations**: RF current generates spin torques (τ_{DL}, τ_{FL}) and Oersted fields that excite magnetization precession
2. **Detect magnetic response**: Through anisotropic magnetoresistance (AMR), oscillating magnetization modulates device resistance, producing a measurable DC voltage when mixed with the driving RF current

The technique's power lies in separating different spin torque contributions through their distinct lineshape signatures: symmetric Lorentzians arise from field-like torques, while anti-symmetric Lorentzians arise from damping-like torques. This allowd us to extract spin Hall angles and spin torque efficiencies as well, on top of finding the H_0 and α, as we did in FMR.

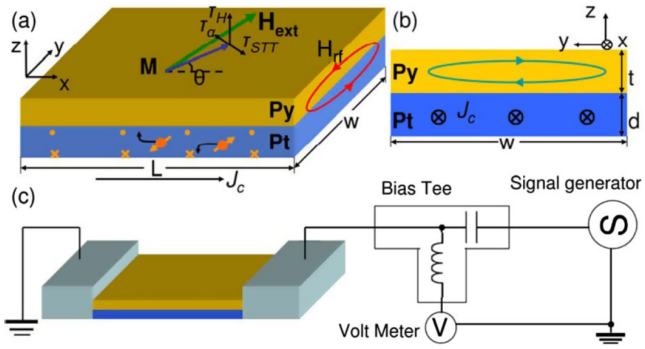

Figure 5.9: (a) The Pt/Py thin film shows three torques: spin-transfer torque (STT), Oersted field torque, and damping torque. The spin Hall effect in Pt generates a spin current into Py, affecting its magnetization. (b) Side view illustrates the Oersted field from current in Py, which doesn't alter Py's anisotropic magnetoresistance. (c) A circuit schematic outlines the setup for spin-torque ferromagnetic resonance (ST-FMR) measurements (source: [7]).

5.5.2 Modified LLG Equation (LLGS Equation)

The magnetization dynamics in ST-FMR are governed by the modified LLG equation:

$$\frac{d\hat{m}}{dt} = -\gamma(\hat{m} \times \vec{H}_{eff}) + \alpha\hat{m} \times \frac{d\hat{m}}{dt} + \vec{\tau}_{DL} + \vec{\tau}_{FL} - \gamma\hat{m} \times \vec{H}_{rf}$$

Where, the first two terms are from LLG itself,

$$\vec{\tau}_{DL} = \gamma \frac{\hbar}{2e\mu_0 M_s t_F} \xi_{DL} J_{C,rf} (\hat{m} \times \hat{\sigma} \times \hat{m})$$

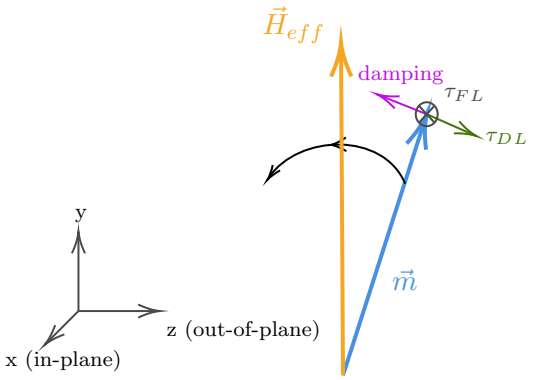

Figure 5.10: Direction of Field-Like and Damping like torques for LLGS (Inspiration: [18]).

is the damping like torque that acts in-plane (see Figure 5.10). It is capable of flipping the FM's magnetization, and hence is of great interest. The other term,

$$\vec{\tau}_{FL} = -\gamma \frac{\hbar}{2e\mu_0 M_s t_F} \xi_{FL} J_{C,rf} (\hat{\sigma} \times \hat{m})$$

is the field like torque that acts out of plane, like the applied field does and the last term $-\gamma \hat{m} \times \vec{H}_{rf}$ is thet Oersted field torque from RF current itself (see Figure 5.9).

5.5.3 Complete Derivation of the Fitting Equation

Step 1: Small-angle approximation and coordinate system

Assuming magnetization primarily along $\hat{y}$ (see Figure 5.10) with small deviations: $\vec{m} = m_x \hat{x} + (1)\hat{y} + m_z \hat{z}$ where $m_x, m_z \ll 1$. Hence we can expand the LLGS by components with $m_y \approx 1$ and $\frac{dm_y}{dt} \approx 0$ as:

$$\frac{dm_x}{dt} = \gamma M_{eff} m_z + \gamma m_z H_{ext} + \alpha \frac{dm_z}{dt} + \tau_x$$

$$\frac{dm_z}{dt} = -\gamma m_x H_{ext} - \alpha \frac{dm_x}{dt} + \tau_z$$

where $\tau_x = |\vec{\tau}_{DL}| \cos\phi$ (in-plane) and $\tau_z = |\vec{\tau}_{FL} - \gamma \hat{m} \times \vec{H}_{rf}| \cos\phi$ (out-of-plane) and ϕ is the angle that the in-plane magnetization is making with the spin current. Just imagine of it as the other spin incoming and it's orientation causing torque on our magnetization vector, then we are looking at it's components.

Step 2: Second-order differential equation

Taking second derivatives of these two equations, we find:

$$\frac{dm_x^2}{dt^2} = \gamma M_{\text{eff}} \frac{dm_z}{dt} + \gamma H_{\text{ext}} \frac{dm_z}{dt} + \alpha \frac{d^2 m_z}{dt^2} + \frac{d\tau_z}{dt}$$

$$\frac{d^2 m_z}{dt^2} = -\gamma H_{\text{ext}} \frac{dm_z}{dt} - \alpha \frac{d^2 m_x}{dt^2} + \frac{d\tau_z}{dt}$$

now replace the $\frac{d^2 m_z}{dt^2}$ and $\frac{dm_z}{dt}$ terms in $\frac{dm_x^2}{dt^2}$ to get:

$$(1+\alpha^2)\frac{d^2m_x}{dt^2}+\gamma\alpha\left(M_{\text{eff}}+2H_{\text{ext}}\right)\frac{dm_x}{dt}+\gamma^2H_{\text{ext}}\left(M_{\text{eff}}+H_{\text{ext}}\right)m_x$$
$$-\gamma\left(M_{\text{eff}}+H_{\text{ext}}\right)\tau_z-\alpha\frac{d\tau_z}{dt}-\frac{d\tau_x}{dt}=0 \tag{5.63}$$

then neglect α^2 and $\alpha\frac{d\tau_z}{dt}$ terms since damping and change in field like torque are negligible, just to get:

$$\frac{d^2m_x}{dt^2}+\gamma\alpha(M_{eff}+2H_{ext})\frac{dm_x}{dt}+\gamma^2H_{ext}(M_{eff}+H_{ext})m_x=\gamma(M_{eff}+H_{ext})\tau_z+\frac{d\tau_x}{dt}$$

Step 3: Harmonic solution

For RF driving at frequency ω: $m_x=m_x^0e^{i\omega t}$, $\tau_x=\tau_x^0e^{i\omega t}$, $\tau_z=\tau_z^0e^{i\omega t}$.
Putting the same in the last equation would give us:

$$-\omega^2m_y+i\omega\gamma\left(M_{\text{eff}}+2H_{\text{ext}}\right)m_y+\gamma^2H_{\text{ext}}\left(M_{\text{eff}}+H_{\text{ext}}\right)m_y$$
$$-\gamma\left(M_{\text{eff}}+H_{\text{ext}}\right)T_z=i\omega\rho^s=0 \tag{5.64}$$

So just solve it for m_x^0 to get:

$$m_x^0=\frac{1}{\omega^2-\omega_0^2-i2\omega\Delta\omega}\left(\omega_z\tau_z^0+i\omega\tau_x^0\right)$$

where $\omega_0=\gamma\sqrt{H_{ext}(M_{eff}+H_{ext})}$, $\omega_z=\gamma(M_{eff}+H_{ext})$, and $\Delta\omega=\frac{1}{2}\alpha\gamma(M_{eff}+2H_{ext})$.

Step 4: Near-resonance approximation

Using $\omega\approx\omega_0$ near resonance:

$$m_x^0=\frac{1}{2}\frac{1}{\omega-\omega_0-i\Delta\omega}\left(\frac{\omega_z}{\omega}\tau_z^0+i\tau_x^0\right)$$

If we then extract the real part of m_x^0 we get the in-phase component of the phase since the imaginary part contains phase lag due to damping/torques. So basically in-phase piece means the part of that oscillation that is synchronous with the driving current $I(t)$. We take the real part (the in-phase component) because it is the only part that produces a measurable, non-zero DC voltage when mixed with the RF current. The imaginary part (the out-of-phase, or quadrature, component) averages to zero over time and is therefore undetectable in our DC measurement. $\Im(m_{x_0})=m''$ represents the component that is 90^o out-of-phase (in quadrature) with the driving torque. It responds as $\Im(m_{x_0})\sin(\omega t)$. Hence:

$$\text{Re}[m_x^0]=\frac{1}{2}\frac{\omega-\omega_0}{(\omega-\omega_0)^2+\Delta\omega^2}\frac{\omega_z}{\omega}\tau_z^0-\frac{1}{2}\frac{\Delta\omega}{(\omega-\omega_0)^2+\Delta\omega^2}\tau_x^0 \tag{5.65}$$

We will explain why we did so, and use this result, just in a moment.

Step 5: Mixing voltage

The device resistance in our case depends on the angle between current and magnetization due to anisotropic magnetoresistance (AMR). When an rf current I_{rf} drives the device, the magnetization precesses at the same frequency, causing the resistance to oscillate as $R(t)=R_0+\Delta R\cos(\omega t+\phi)$. The product of the oscillating current and resistance produces a rectified dc component, called the mixing voltage. Lets say, the rf current and resistance be

$$I(t) = I_{\rm rf}\cos(\omega t), \qquad R(t) = R_0 + \Delta R\cos(\omega t + \phi).$$

The instantaneous voltage is

$$V(t) = I(t)R(t) = I_{\rm rf}R_0\cos(\omega t) + I_{\rm rf}\Delta R\cos(\omega t)\cos(\omega t + \phi).$$

Using

$$\cos A\cos B = \tfrac{1}{2}\big[\cos(A-B) + \cos(A+B)\big],$$

we obtain

$$V(t) = I_{\rm rf}R_0\cos(\omega t) + \tfrac{1}{2}I_{\rm rf}\Delta R\cos\phi + \tfrac{1}{2}I_{\rm rf}\Delta R\cos(2\omega t + \phi).$$

Taking the time average (DC component) removes all oscillatory terms:

$$\langle V(t)\rangle = \tfrac{1}{2}I_{\rm rf}\Delta R\cos\phi.$$

Since $\cos\phi$ is the in-phase (real) component of ΔR, we write

$$V_{\rm mix} = \tfrac{1}{2}I_{\rm rf}\,{\rm Re}(\Delta R). \tag{5.66}$$

which is the experimentally measurable signal in ST-FMR. Imagine a resistance component driven by the quadrature (imaginary) response:

$$\delta R_{\rm imag}(t) \propto \cos(\omega t); \qquad [\because \sin(\omega t + 90^o) = \cos(\omega t)].$$

Now mix it with the current $I(t) = I_{\rm rf}\sin(\omega t)$:

$$V_{\rm mix,\ imag} = \langle I_{\rm rf}\sin(\omega t)\cdot{\rm const}\cdot\cos(\omega t)\rangle_t = {\rm const}\cdot I_{\rm rf}\langle\sin(\omega t)\cos(\omega t)\rangle_t$$

The time-average of $\sin(\omega t)\cos(\omega t)$ is zero. Therefore: $V_{\rm mix,\ imag} = 0$. Hence, we can ignore the imaginary component, as it produces no net DC voltage over one full cycle.

Also note that,

$$\delta R = \frac{dR}{d\phi}\delta\phi \approx -\frac{dR}{d\phi}{\rm Re}[m_x^0]\sin(\omega t),$$

since in small-angle precession, the in-plane angle change $\delta\phi$ (the rotation of magnetization in the film plane) is directly proportional to the x-component of the magnetization m_x.

This gives the mixing voltage from (5.66) and (5.65) in field-sweep form:

$$V_{mix} = -\frac{1}{4}I_{rf}\frac{dR}{d\phi}\frac{1}{\Delta H}\left(\frac{d\omega}{dH}\right)^{-1}_{H=H_0}\left[F_A(H)\tau_z^0\sqrt{\frac{M_{eff}}{H_0}+1} - F_S(H)\tau_x^0\right] \tag{5.67}$$

where $F_S(H) = \frac{\Delta H^2}{(H-H_0)^2+\Delta H^2}$ and $F_A(H) = \frac{(H-H_0)\Delta H}{(H-H_0)^2+\Delta H^2}$ are symmetric and antisymmetric Lorentzians. $\Delta H = \omega\gamma/\alpha$, is the convention to say ΔH as HWHM unlike how we have declared it as FWHM so far.

Step 6: Final parametrization in Standard Terminology

Defining:

$$S = \frac{1}{\gamma}\tau_{DL} = \frac{\hbar}{2e\mu_0 M_s t_F}\xi_{DL} J_{C,rf} = H_{DL}$$

$$A\frac{1}{\sqrt{M_{eff}/H_0 + 1}} = \frac{\hbar}{2e\mu_0 M_s t_F}\xi_{FL} J_{C,rf} + \frac{t_N J_{C,rf}}{2} = H_{FL} + H_{rf}$$

The mixing voltage becomes:

$$\boxed{V_{mix} = -\frac{1}{2}\gamma I_{rf} R_{AMR} \sin\phi \cos^2\phi \frac{1}{\Delta H}\left(\frac{d\omega}{dH}\right)^{-1}_{H=H_0}(SF_S(H) + AF_A(H))} \tag{5.68}$$

using, $\frac{dR}{d\phi} = -2\sin(\phi)\cos(\phi)R_{AMR}$, with $R_{AMR} = (R_{\parallel} - R_{\perp})$, which we can get by differentiating (5.2).

Step 7: Spin-to-charge current ratio

In the absence of field-like torque beyond Oersted field, we can define the efficiency of FMR as:

$$\boxed{\xi_{FMR} \equiv \frac{J_{S,rf}}{J_{C,rf}} = \frac{S}{A}\frac{e\mu_0 M_s t_F t_N \sqrt{M_{eff}/H_0 + 1}}{\hbar}} \tag{5.69}$$

This fundamental equation from [7] provides the baseline ST-FMR fitting function (modified to more parameters, than discussed in paper, as per [18]), relating the measurable symmetric-to-antisymmetric ratio to the spin torque efficiency. It assumes no additional effects like spin pumping, which would require further modifications to account for dynamic spin current backflow from ferromagnet to normal metal.

Note: We have ignore field like torque in our calculation, however, Adding a thin 0.3 nm Hf spacer layer at the Pt/FeCoB interface, however, has been shown to suppress the field-like torque and hence, very benificial for our measurements [11] [18].

5.6 Practical Fitting and Extraction of Parameters from ST-FMR Measurements

Lets lay out the basic equation for the standard ST-FMR analysis, the mixing voltage, which has the form as in (5.68).

$$V_{mix} = -\frac{1}{2}\gamma I_{rf} R_{AMR} \sin\phi \cos^2\phi \frac{1}{\Delta H}\left(\frac{d\omega}{dH}\right)^{-1}_{H=H_0}(SF_S(H) + AF_A(H))$$

Where:

- $F_S(H) = \frac{\Delta H^2}{(H-H_0)^2+\Delta H^2}$ is the **symmetric Lorentzian**
- $F_A(H) = \frac{(H-H_0)\Delta H}{(H-H_0)^2+\Delta H^2}$ is the **antisymmetric Lorentzian**

Parameter Extraction Process:

1. **Linewidth and Damping (α)**:
   - From the HWHM of the resonance: $\Delta H = \frac{\alpha\omega}{\gamma}$
   - Measure linewidth vs. frequency to extract damping: $\Delta H = \Delta H_0 + \frac{2\pi\alpha f}{\gamma}$
   - The slope gives α, intercept gives inhomogeneous broadening ΔH_0
2. **Resonance Field and Effective Magnetization**:
   - At resonance: $\omega_0 = \gamma\sqrt{H_0(M_{eff} + H_0)}$
   - Plot $(f/\gamma)^2$ vs H_0 → slope and intercept give M_{eff}
3. **Spin Torque Efficiencies**:
   - The symmetric amplitude S relates to damping-like torque:
   $$S = \frac{\hbar}{2e\mu_0 M_s t_F}\xi_{DL} J_{C,rf} \tag{5.70}$$
   - The antisymmetric amplitude A relates to field-like torque + Oersted field:
   $$A\frac{1}{\sqrt{M_{eff}/H_0 + 1}} = \frac{\hbar}{2e\mu_0 M_s t_F}\xi_{FL} J_{C,rf} + \frac{t_N J_{C,rf}}{2} \tag{5.71}$$
4. **Fitting Procedure**:
   - Fit the voltage spectrum to: $V = V_S F_S(H) + V_A F_A(H)$
   - Extract V_S and V_A amplitudes
   - Calculate the ratio: $\frac{S}{A} = \frac{V_S}{V_A}\sqrt{1 + M_{eff}/H_0}$
   - This gives the ST-FMR efficiency:
   $$\xi_{FMR} = \frac{S}{A}\frac{e\mu_0 M_s t_F t_N\sqrt{M_{eff}/H_0 + 1}}{\hbar} \tag{5.72}$$
5. **Thickness Dependence Analysis**:
   - Without field-like torque: $\xi_{FMR} = \xi_{DL}$
   - With field-like torque: $\frac{1}{\xi_{FMR}} = \frac{1}{\xi_{DL}} + \frac{\hbar}{e\mu_0 M_s t_F t_N}\frac{\xi_{FL}}{\xi_{DL}}$
   - Plot $1/\xi_{FMR}$ vs $1/(t_F t_N)$ → intercept gives $1/\xi_{DL}$, slope gives ξ_{FL}/ξ_{DL}

5.7 Factoring for Spin Pumping Correction

Spin pumping creates an additional DC voltage that was being ignored. During FMR, the precessing magnetization pumps a pure spin current into the adjacent normal metal, which gets converted back to a charge current via the inverse spin Hall effect (ISHE), as discussed in section 5.3. This creates a voltage that **opposes** the ST-FMR signal.

- **ST-FMR signal**: RF current → spin current (via SHE) → torque on FM → resistance oscillation → DC voltage
- **Spin pumping signal**: Magnetization precession → spin current pumped into NM → charge current (via ISHE) → DC voltage

The spin pumping voltage has **opposite sign** to the ST-FMR symmetric component, causing systematic underestimation of torques.

Ryan Christopher Tapping's Thesis [18] is mainly focused on testing out this impact of Spin pumping on ST-FMR, and incorporating for these extra factors introduced. We will directly discuss these results briefly here.

Spin Pumping Voltage Derivation

The spin pumping voltage contributes only a **symmetric component**:

$$V_{SP} = \frac{1}{4} R_{y'} \sin\phi \cos^2\phi \frac{1}{\Delta H} \left(\frac{\partial \omega}{\partial H} \right)^{-1}_{H=H_0} \theta_{SH} \frac{e}{2\pi} w \lambda_N g_e^{\uparrow\downarrow} F_S(H) \times \frac{1}{\Delta\omega} \left[\omega_z (\tau_{FL} + \tau_{Oe})^2 + \omega_x \tau_{DL}^2 \right] \tanh\left(\frac{t_N}{2\lambda_N} \right) \tag{5.73}$$

Where:

- $g_e^{\uparrow\downarrow}$ = effective spin mixing conductance
- λ_N = spin diffusion length in NM
- θ_{SH} = spin Hall angle

Modified Total Voltage

The total measured voltage becomes:

$$V_{total} = V_{mix} + V_{SP} = -\frac{1}{2} \gamma I_{rf} R_{AMR} \sin\phi \cos^2\phi \frac{1}{\Delta H} \left(\frac{d\omega}{dH} \right)^{-1}_{H=H_0} (S' F_S(H) + A F_A(H)) \tag{5.74}$$

Where the modified symmetric amplitude is:

$$S' = S - \xi_{DL}^{SP} \Gamma \left[\left(1 + \frac{\hbar}{e\mu_0 M_s t_F t_N} \xi_{FL} \right) A + \left(\frac{\hbar}{e\mu_0 M_s t_F t_N} \xi_{DL} \right) \frac{H_0}{\sqrt{H_0(M_{eff} + H_0)}} S \right] \tag{5.75}$$

The Correction Factor Γ

$$\Gamma = \exp\left(-\frac{t_{Hf}}{\lambda_{Hf}} \right) \frac{\sigma_F t_F}{\sigma_N t_N + \sigma_F t_F} \frac{R_{y'}}{R_{AMR}} \frac{h}{e} \frac{\gamma}{8\pi\rho_N} \frac{1}{\alpha} \frac{\sqrt{H_0(M_{eff} + H_0)}}{M_{eff} + 2H_0} \tanh\left(\frac{t_N}{2\lambda_N} \right) \tag{5.76}$$

This factor encapsulates:

- Current shunting between layers
- Spin diffusion and relaxation
- Interface transparency effects

Modified Efficiency with Spin Pumping

The measured ST-FMR efficiency becomes:

$$\xi_{FMR} = \xi_{DL} \left(\frac{1}{1 + \frac{C_2}{t_F t_N} \xi_{FL}} \right) \times \left(1 - \frac{\xi_{DL}^{SP}}{\xi_{DL}} \Gamma \left(C_1 t_F t_N + 2 C_1 C_2 \xi_{FL} + C_1 C_2^2 t_F t_N \xi_{FL}^2 + \xi_{DL}^2 C_1 t_F t_N \right) \right) \tag{5.77}$$

Where:

- $C_1 = \frac{e\mu_0 M_s \sqrt{M_{eff}/H_0 + 1}}{\hbar}$
- $C_2 = \frac{\hbar}{e\mu_0 M_s}$

5.8 Setup and Lithography

Physical Device Fabrication

ST-FMR devices are made on wafers with a pre-sputtered Pt/Py bilayer. The film thickness can vary by about 10–15% from the center to the edges, which is important for accurate spin torque measurements. The devices are patterned using two lithography steps with a positive photoresist, which is spin-coated and exposed by photolithography to define the active regions.

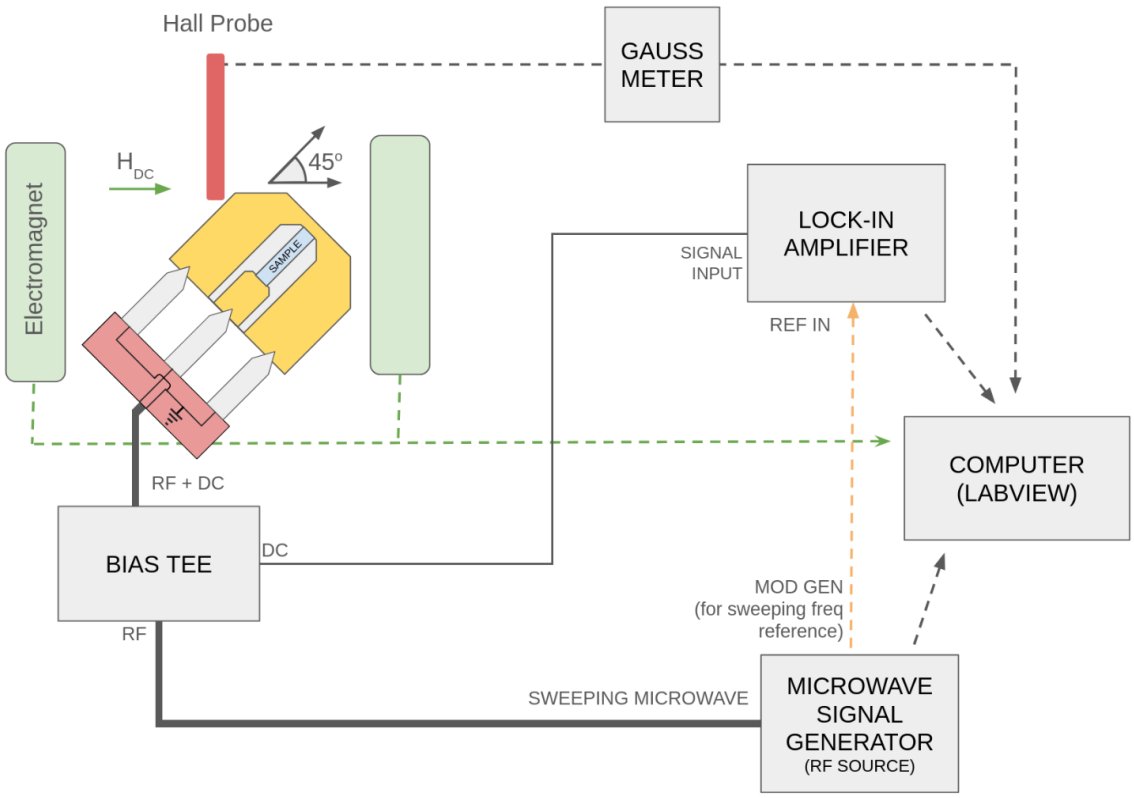

Figure 5.11: Block diagram for the ST-FMR experimental setup showing the complete measurement chain. Sample is deposited on Pt/Py bilayer. The device under test is positioned at 45^o to the applied magnetic field H, with RF drive current supplied through a bias tee that simultaneously enables DC voltage detection. A microwave signal generator provides both the RF excitation and low-frequency modulation reference for lock-in detection, while a Hall probe monitors the field strength during magnetic field sweeps. The lock-in amplifier extracts the weak ST-FMR mixing voltage from noise, with all components coordinated through computer control for automated data acquisition.

After developing the photoresist, ion beam etching transfers the pattern into the magnetic stack. Accelerated ions remove material by sputtering, producing sharp device edges. The process slightly over-etches to avoid electrical shorts, with the insulation layer protecting the stack. The photoresist is then removed by solvent cleaning and ultrasonic treatment [18].

The second lithography step defines contact pads, aligned with the etched features. After resist patterning and cleaning, contact pads (usually Ti/Pt) are added by physical vapor deposition to provide low-resistance microwave contacts. Finally, extended solvent treatment removes the unwanted metal layers.

Device Architecture and Measurement Configuration

The finished devices are rectangular bars of $20 \times 10\,\mu m^2$ with ground-signal-ground pads for coplanar waveguide probing. They are placed on the wafer in a grid, with some areas left unpatterned as control samples for magnetic tests. The geometry forms a coplanar waveguide with controlled impedance for high-frequency measurements [18]. The ST-FMR setup uses lock-

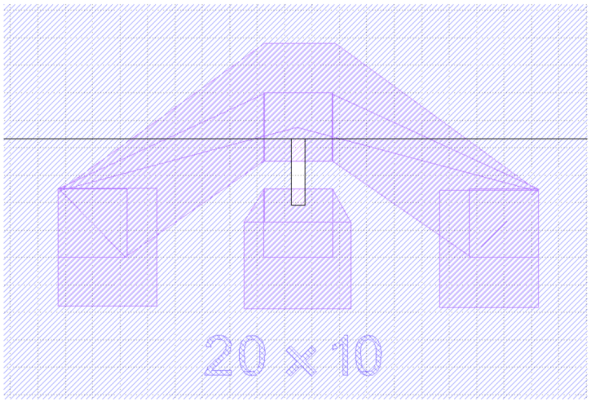

Figure 5.12: Close-up of the layout for the hall bar and contact pad used specifically for ST-FMR in [18].

in detection. A microwave generator provides the RF drive modulated at some low frequency, coupled through a bias tee that also allows DC voltage measurement. The bias tee separates the high-frequency drive from the low-frequency mixing voltage (the ST-FMR signal). A Hall probe monitors the magnetic field, while an electromagnet sweeps the DC field.

The key feature is the lock-in amplifier. The microwave source also supplies a low-frequency modulation reference (tens to hundreds of Hz) to the lock-in, which extracts the weak ST-FMR mixing voltage from noise. A computer synchronizes the field sweep with data collection to build the full resonance spectrum.

Angular Geometry and Lock-in Detection Principles

The 45° angle between the magnetic field and the current serves two main purposes. It maximizes anisotropic magnetoresistance sensitivity, since $dR/d\phi$ is largest when the magnetization is at 45° to the current. It also breaks symmetry between torque effects, allowing the symmetric Lorentzian part (from spin-transfer torque) to be separated from the antisymmetric part (from Oersted fields) [7].

Lock-in detection modulates the microwave frequency at a low reference (20–200 Hz). This slightly shifts the resonance, producing a small mixing voltage oscillating at the same frequency. The lock-in amplifier detects this tiny oscillation while rejecting noise, interference, and drift, enabling microvolt-level sensitivity to the weak ST-FMR signal.

Technical Implementation and Signal Analysis

The setup needs precise impedance matching and grounding to keep signals clean from DC to microwave frequencies. The ground-signal-ground probe ensures proper transmission line behavior, while the bias tee must isolate RF and DC paths over a wide range. Temperature stability and vibration isolation are critical, since thermal and mechanical noise can hide the microvolt-level ST-FMR signal.

Data analysis fits the resonance curves with symmetric and antisymmetric Lorentzian terms. Their ratio gives the spin current efficiency. The same has been discussed in section 5.6.

Bibliography

[1] Infineon Technologies AG. *RF and Microwave Power Detection with Schottky Diodes*. Tech. rep. AN_1807_PL32_1808_132434. Last accessed: Aug 2024. Available at infineon.com. Infineon Technologies, July 2018.

[2] Saurabh Basu. *Topological Phases in Condensed Matter Physics*. Springer Nature Singapore, 2023. ISBN: 9789819953219. DOI: 10.1007/978-981-99-5321-9.

[3] Vegard Flovik et al. "Eddy current interactions in a ferromagnet-normal metal bilayer structure, and its impact on ferromagnetic resonance lineshapes". In: *Journal of Applied Physics* 117.14 (Apr. 2015). ISSN: 1089-7550. DOI: 10.1063/1.4917285.

[4] J. T. van Galen. "Building a Ferromagnetic Resonance Setup". In: (2017).

[5] Daniella Goldfarb. *Series of EPR Lectures*. Recorded by the Australia and New Zealand Society for Magnetic Resonance at the EPR Workshop. Lecture series PDF: EPR spectrometer. 2014.

[6] Charles Kittel and Paul McEuen. *Introduction to Solid State Physics*. en. New York, NY: John Wiley & Sons, 2018.

[7] Luqiao Liu et al. "Spin-Torque Ferromagnetic Resonance Induced by the Spin Hall Effect". In: *Physical Review Letters* 106.3 (2011), p. 036601. DOI: 10.1103/PhysRevLett.106.036601.

[8] Luqiao Liu et al. "Spin-Torque Switching with the Giant Spin Hall Effect of Tantalum". In: *Science* 336.6081 (2012), pp. 555–558. DOI: 10.1126/science.1218197.

[9] Naoto Nagaosa et al. "Anomalous Hall effect". In: *Reviews of Modern Physics* 82.2 (May 2010), pp. 1539–1592. ISSN: 1539-0756. DOI: 10.1103/revmodphys.82.1539.

[10] Application Note. "3. About Lock-in Amplifiers". In: *Stanford Research Systems, Scientific and Engineering Instruments* 1993 (1992), p. 129.

[11] Yongxi Ou et al. "Origin of fieldlike spin-orbit torques in heavy metal/ferromagnet/oxide thin film heterostructures". In: *Phys. Rev. B* 94 (14 Oct. 2016), p. 140414. DOI: 10.1103/PhysRevB.94.140414.

[12] D.A. Petukhov. "Spin-polarized current and tunnel magnetoresistance in heterogeneous single-barrier magnetic tunnel junctions". In: *Physica E: Low-dimensional Systems and Nanostructures* 80 (2016), pp. 31–35. ISSN: 1386-9477. DOI: https://doi.org/10.1016/j.physe.2016.01.009.

[13] D. Polder. "On the theory of ferromagnetic resonance". In: *Physica* 15.1 (1949), pp. 253–255. ISSN: 0031-8914. DOI: 10.1016/0031-8914(49)90051-8.

[14] S. Sachdev. *Quantum Phases of Matter*. Cambridge University Press, 2023. ISBN: 9781009212694.

[15] Ivan Soc and Eamon Nash. *AN-2061: Wideband Bias Tee Design Using 0402, SMD Components*. Tech. rep. AN-2061. Application Note. Analog Devices, 2023.

[16] Michael Steer. *Microwave and RF Design II: Transmission Lines*. Available at commons.libretexts.org. North Carolina State University, 2020.

[17] Stanford Research Systems. *SR830 DSP Lock-In Amplifier*. Accessed: 2025-08-17. 2025.

[18] Ryan Christopher Tapping. "Additional Sources to the Signal: Spin Pumping in Spin Torque Ferromagnetic Resonance and Student-Level Variables in Linear Mixed-Effects Models". Accessed August 2025. Available at ecommons.cornell.edu. Ph.D. dissertation. Cornell University, Dec. 2021.

[19] David Tong. *Lectures on the Quantum Hall Effect*. 2016. DOI: arXiv:1606.06687.

[20] T. Valet and A. Fert. "Theory of the perpendicular magnetoresistance in magnetic multilayers". In: *Phys. Rev. B* 48.10 (Sept. 1993), pp. 7099–7113. DOI: 10.1103/PhysRevB.48.7099.

[21] Dahai Wei et al. "Spin Hall voltages from a.c. and d.c. spin currents". In: *Nature Communications* 5 (2014), p. 3768. DOI: 10.1038/ncomms4768.

[22] Orhan Yalçın. "Ferromagnetic Resonance". In: *Ferromagnetic Resonance*. Ed. by Orhan Yalcin. Rijeka: IntechOpen, 2013. Chap. 1. DOI: 10.5772/56134.

[23] J. M. Ziman. *Principles of the Theory of Solids*. Second Edition. Cambridge University Press, 1972. ISBN: 9780521083826.

[24] Zurich Instruments. *Principles of Lock-in Detection and the State of the Art*. White Paper. Last updated April 2023. Zurich Instruments, May 2023.